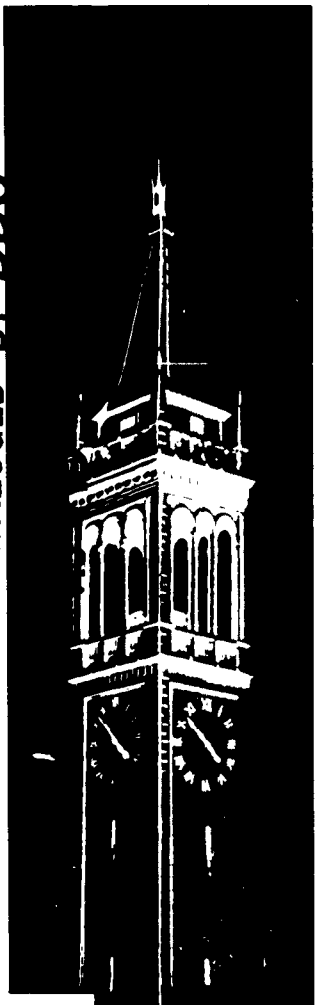

Three-Level Maser Materials: A Survey of Potential Materials, II

by

J. Wakabayashi

Series No. 60, Issue No. 452
Contract No. AF 49(638)-102
June 1, 1962

ELECTRONICS RESEARCH LABORATORY

UNIVERSITY OF CALIFORNIA
BERKELEY, CALIFORNIA

Electronics Research Laboratory
University of California
Berkeley, California

THREE-LEVEL MASER MATERIALS: A SURVEY OF POTENTIAL MATERIALS, II

by

J. Wakabayashi

Institute of Engineering Research
Series No. 60, Issue No. 452

Physics Division
Air Force Office of Scientific Research
Contract No. AF 49(638)-102
Division File No. 13-25-J

June 1, 1962

ABSTRACT

Paramagnetic resonance of impurities in natural crystals of calcite ($CaCO_3$) and barite ($BaSO_4$) were investigated. Observed spectra are compared with the theoretical spectra of probable impurities. One spectrum in calcite is identified with Fe^{3+}. Another is possibly due to Cr^{3+}. No identifiable spectrum was observed in barite.

TABLE OF CONTENTS

INTRODUCTION

Current research in microwave masers can be classified into two categories.

1. Research in the maser as a device. This involves research in the actual design, construction and application of the microwave maser.
2. Research in maser materials. This involves the search for maser materials which would be superior to presently known materials in performance or which would allow the construction of a maser in a frequency range not permitted by currently known materials. The emphasis, of course, is in obtaining materials which are suitable for higher frequencies.

The investigations reported here fall in the second category. The two materials which are currently prominent in microwave masers are ruby ($Al_2O_3:Cr^{3+}$) and rutile (TiO_2) with Fe^{3+} impurity. Ruby has been a very successful material. However, the range of frequency in which it can be used is limited to below approximately 10 gc. This is determined by the zero-field splitting in the material which is 12 gc. Rutile is much more versatile. It has been used in experimental masers in the 36 gc. range and at higher frequencies.[11] Ruby is an excellent material in its frequency range. It is not yet clear whether TiO_2 is as good in its higher frequency range.

The merits of a maser material are determined by a number of factors which are discussed in a companion report, ERL

Technical Report, Series No. 60, Issue No. 439. They are:

1. long energy relaxation times (T_1)
2. narrow resonance band-width (T_2)
3. appropriate zero-field splitting
4. equivalence of paramagnetic impurity sites
5. physical stability

A survey of potential maser materials was given in the companion report.

Most of the crystals which appear to be promising are not available synthetically. Natural samples are available for many of the crystals, but the quality of most of them is too poor for investigation. However, excellent natural crystals are available for two materials. They are calcite ($CaCO_3$) and barite ($BaSO_4$). Many samples of calcite are good enough to use in optical equipment. Barite is available in excellent single crystals which attain a weight of as much as a hundred pounds. Good samples of either have negligible impurities. The resistivity is extremely high for good samples. One disadvantage of both materials is that the paramagnetic impurities occupy two non-equivalent sites. This leads to two distinct resonance spectra instead of one. For a general orientation of the magnetic field only one of the sites would be resonant at a particular frequency. Therefore, only half of the paramagnetic impurities participate in the maser action. However, in both cases the sites are equivalent when the magnetic field is parallel to special symmetry planes in the crystal. Variation of the magnetic field direction

within these special planes still provides sufficient flexibility in energy levels to make them potentially useful for maser applications if the material has merit otherwise. Therefore, it was considered worthwhile to investigate these two materials as maser materials. There is very little chance of natural crystals being considered in practical masers. However, if the results of this investigation revealed a crystal to be very promising, it might spur efforts to grow it synthetically.

The investigation of the crystals as maser materials involves the following:

1. Addition of paramagnetic impurities to the crystals.
2. Measurement of the paramagnetic resonance spectrum to determine the spin-Hamiltonian.
3. Measurement of the relaxation times and line widths of the paramagnetic resonances.

The first step, that of inclusion of impurities, was to be accomplished by diffusion. This was attempted by heating the crystals with the impurity salt powder or by heating crystals plated with the impurity to be diffused. It was not successful. The investigation was then shifted to naturally existing impurities. The concentrations of these impurities was low. This led to experimental limitations which resulted in poor accuracy.

As the result of the investigation the paramagnetic spectrum of Fe^{3+} in calcite and probably that of Cr^{3+} has been identified. The parameters of the spin-Hamiltonian is given in each case. The values are not very precise. No interesting

spectrum was identified in barite.

The results of the investigation, even with the inaccuracies, show that Fe^{3+} in calcite does not have a very large zero-field splitting. Therefore, it is not suited to high frequency masers. It has possibilities in the low microwave region, but even there it does not show any advantage over ruby. It is certain that any effort towards the synthesis of calcite would be motivated by optical applications rather than masers.

CHAPTER 1

EXPERIMENTAL PROCEDURE AND EQUIPMENT

1.1 Paramagnetic Resonance Measurement

The equipment and scheme used for the detection of paramagnetic resonance measurements are very similar to the scheme used for a maser with a reflection cavity. In the case of the maser amplifier, the increase in reflection from the cavity is detected. In a simple resonance, the decrease in reflection due to resonant absorption in the cavity is detected. A block diagram of the experimental equipment is given in Fig. 1.

Microwave field from the frequency-stabilized source is fed into a "magic-T" via an isolator and a variable attenuator. Half of the microwave energy entering the bridge enters the absorption cavity which is located between the pole pieces of the magnet. This cavity is spatially resonant to the microwave frequency. The other half is fed to a load of variable phase and magnitude. This is referred to as the bucking arm. In the absence of magnetic resonance absorption, a reflection $\bar{\Gamma}_o$ occurs at the cavity. This reflection is dependent on the impedance match between the cavity and waveguide. The phaser difference between the reflection from the cavity and the variable load on the opposite arm of the "magic-T" is detected by the crystal on the detector arm.

When the magnetic field is varied so that paramagnetic resonance occurs within the cavity, the impedance of the cavity changes, and the reflection from the cavity is increased or

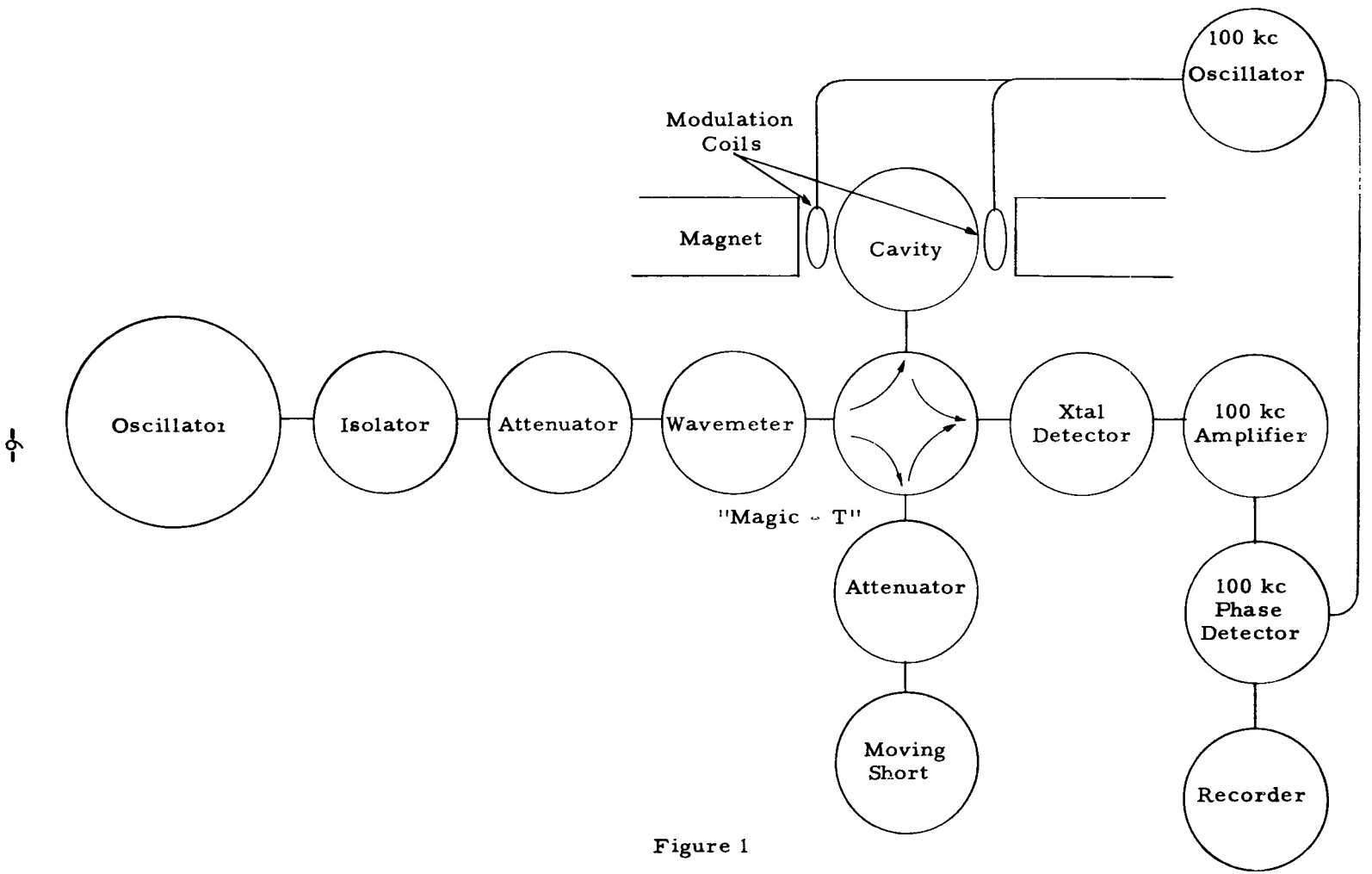
100 kc
Oscillator
Modulation
Coils
Magnet
Cavity
Oscillator
Isolator
Attenuator
Wavemeter
Xtal
Detector
100 kc
Amplifier
"Magic - T"
Attenuator
100 kc
Phase
Detector
Moving
Short
Recorder

Figure 1

decreased, depending on whether the cavity was originally under-coupled or over-coupled. The change in reflection coefficient from the value for off-resonance is given by

$$\Delta\Gamma = \frac{2\alpha Q(x'' - jx')}{(\alpha + 1)(\alpha + 1 - 2Qx'')} \tag{1.1}$$

Here $\alpha = R/Z'_o$, where R is the impedance of the cavity without magnetic resonance, and Z'_o is the impedance of the waveguide reflected into the cavity. $x' + jx''$ is the susceptibility of the sample. It is a function of frequency and magnetic field. For paramagnetically dilute samples $Qx'' \ll 1$ so that this factor in the denominator is neglected. Substitution of the values of x' and x'' gives

$$|\Delta\Gamma|^2 \propto x''^2 + x'^2 = \frac{\gamma^2 M_o^2}{\left[(\gamma H_o + \omega)^2 + \frac{1}{T_2^2}\right]} \tag{1.2}$$

where $T_1 = T_2$ and the microwave field strength is assumed to be small compared with $1/T_2$. In fact, $\Delta\Gamma$ describes a circle of radius $\frac{\alpha Q}{(\alpha+1)^2} \cdot \gamma M_o T_2$ as in Fig. 2. As the field starts from 0 and rises to ∞, the locus of $\Gamma = \Gamma_o + \Delta\Gamma$ traces out a circle starting at Γ_o and circling counter-clockwise back to Γ_o. The signal detected by the crystal is the phaser difference between the reflections from the cavity and the bucking arm. This is illustrated in Fig. 3. The particular configuration gives a curve which is a replica of x'' when $|\Gamma_d|$, the detected field, is plotted against magnetic field. This configuration can be

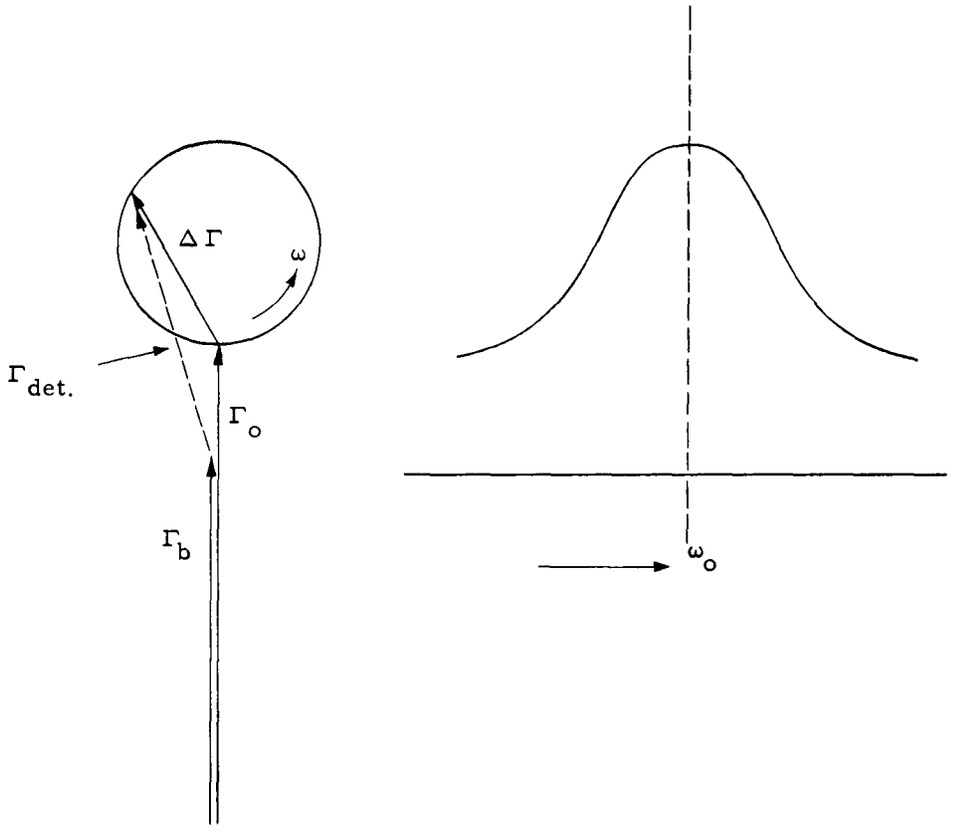

Figure 2

obtained by first adjusting $|\Gamma_d|$ off resonance to either a maximum or minimum by means of the bucking phase. A choice of bucking as in Fig. 3 gives a signal which is a replica of x'. $\Delta\Gamma$ is a small quantity which is essentially d.c. The detection is made difficult because of the inherent instability of d.c. amplifiers which prevents very high gain from being used.

This difficulty is circumvented by imposing an a.c. modulation component on the magnetic field. If the amplitude of this modulation is smaller than the width of the resonance line, an a.c. amplitude modulation appears in $\Delta\Gamma$ which is proportional to the slope of $\Delta\Gamma$: $d(\Delta\Gamma)/d(H_{dc})$. The crystal detects this modulation. This a.c. signal is amplified by a high gain a.c. amplifier. A second detector in the form of a synchronous phase detector sends d.c. signal to a recorder. The phase detector can be made to have a very narrow bandwidth to reduce the noise. The output of the phase detector traces the derivative of x' or x" with respect to H.

The noise in such a resonance detecting system is due to

a) AM noise in the microwave source

b) FM noise in the microwave source

c) Crystal noise

d) Magnetic field instability

AM noise in the source can be reduced by using good klystrons with stable filament and electrode voltages. It is partially removed from the output by balancing the "magic-T" to give maximum cancellation. Ideally, the bridge should be completely balanced so that all source AM is cancelled and only $\Delta\Gamma$ is

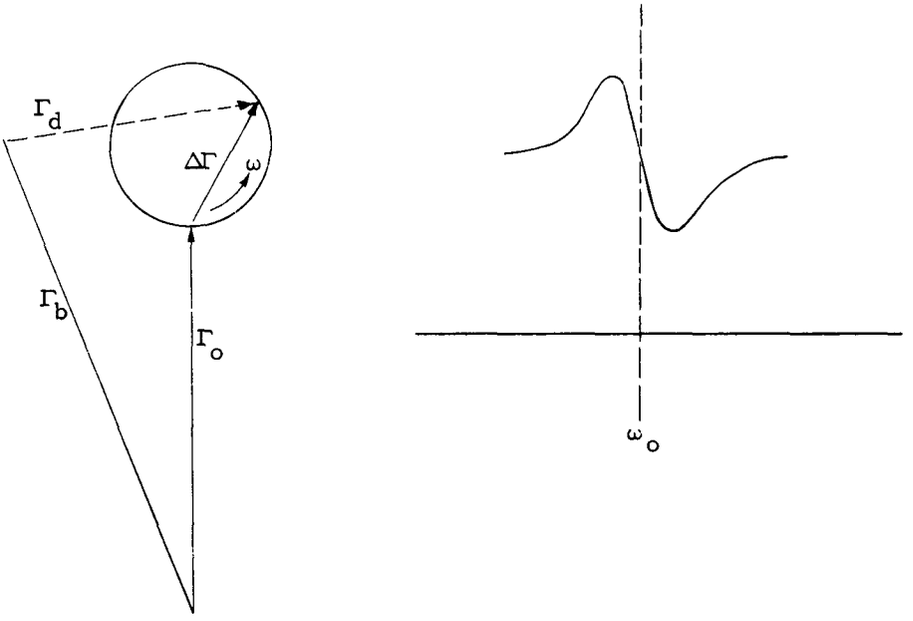

Figure 3

incident on the crystal. However, the crystal output signal drops to zero under this condition because the crystal is a square-law device. Some residual unbalance is required to obtain a non-zero signal output. A crystal biasing current furnished by a stable battery may be one way to avoid the unbalance.

The FM noise in the microwave source is minimized by Automatic Frequency Controls. The effect of FM on paramagnetic resonance is the same as that of magnetic field modulation. Therefore, it is very important to reduce such noise. In addition to its direct effect on resonance, it also adds AM noise to the resonance signal output by slope detection on the microwave cavity resonance. This is naturally more severe when the Q of the cavity is very high.

The detecting crystals contribute a noise which is known experimentally to be proportional to 1/f in power. For a given bandwidth, the noise contribution from the crystal is reduced if a high center frequency is taken. For this reason, a high frequency field modulation frequency is used for sensitive spectrometers. The noise is also reduced by reducing the bias on the crystal.

The stability of the magnetic field is important. Any fluctuating component at the field modulation frequency will give a detectable noise.

1.2 Measurement of Relaxation Times

The measurement of T_2 is made by observing the recorded-line width. The relation between line width and T_2 is

$$\gamma \Delta H = \frac{1}{T_2}$$

for g = 2, it becomes

$$2\pi \times 2.8 \times 10^6 \Delta H = \frac{1}{T_2}$$

This expression should be accurate enough for any line, even when g is not exactly equal to 2 but does not depart from 2 by a great amount.

The measurement of T_1 is much more difficult. There are three methods. The first method makes use of the saturation condition in the solution to Bloch's equation. There, it was noted that x'' at resonance decreases as $\gamma H' > 1/T_1T_2$, where H' is the circularly polarized r.f. amplitude. By increasing the power until saturation is observed by the reduction of the absorption signal to one-half, we can find T_1, provided T_2 and the field H' in the cavity are known. In principle this is as good a method as any and certainly the simplest to apply. T_2 can be taken from the measured line width. H' can be computed by knowing the input power to the cavity, the reflection and the Q of the cavity. In practice, it is not as reliable. The reason is that Bloch's equations are based on all the spins having the identical Larmor frequency. (No spread in γ is included.) It cannot account for inhomogeneous broadening.

Another method for the measurement of T_1 is a pulse method. In this method, a high-powered pulse is applied to the spins to completely saturate the spins. The imaginary susceptibility x'' is zero at saturation and remains zero for a time T_1 even after the pulse is turned off. A low power resonance absorption measurement

is made immediately after the removal of the strong pulse to measure the recovery from saturation. This method has three weaknesses. The thermal effects associated with the sudden change in applied power to the cavity must be isolated. The magnetic field and microwave frequency must be very accurately on resonance and the "magic-T" adjusted exactly to observe just the absorption. Furthermore, a d.c. detection scheme must be used. This requires that the spin concentration be high enough to give sufficient signal with stability. It is also difficult to switch microwave power by the required 40 or 50 db in a short time. The method is not suited for short relaxation times ($T_1 < 10^{-3}$).

The third method for the measurement of T_1 is by spin-echo.[50] This is a more elaborate method both in theory and instrumentation. The principles of spin-echoes will be explained as simply as possible in a classical manner.

When a total spin moment M_0 comprised of many individual moments is oriented normal to the d.c. magnetic field, the moment vanishes in a characteristic time T_2. This is due to a disordering spin-spin interaction process and an ordered destructive interference arising from a variation in the Larmor frequency. They are called homogeneous T_2 and inhomogeneous T_2, respectively. When the inhomogeneous T_2 is much shorter than the homogeneous T_2, the individual spins have a definite predictable position related to their Larmor frequency even after the net transverse moment is zero. By applying a resonant pulse which nutates all the moments by 180° about the applied field, the individual spins can be made to converge to reform a net M_0 at the same rate at which they

diverged to destroy M_o. This will happen as long as the total elapsed time in the transverse plane does not exceed homogeneous T_2. If a detector is set up to observe the transverse moment M_o, a signal will be observed initially when M_o is put in that position, then when a pulse is applied, and for a third time when no pulse is applied but M_o is recreated. This third signal is termed the spin-echo τ.

To obtain a spin-echo, a resonant pulse of amplitude H' is applied for a duration $\tau = \frac{\pi}{2\gamma H'}$. The amplitude should be larger than the line width of the spins. This pulse rotates all the spins by approximately $\pi/2$ from the z-axis to give the transverse M_o. The angle of rotation is determined by the duration, and the participation of all the spins is insured by making $H' > \Delta H$, where ΔH is the line width.

A second pulse is applied in a time Δt after the first pulse. It is of the same amplitude as the first pulse, but the duration is twice as long. This rotates all the spins by an angle π about the pulse field. The echo follows in a time Δt after the second pulse. This process can be used to measure homogeneous T_2 by lengthening Δt until an echo is no longer observed.

A different type of echo is used for the measurement of T_1. In this case, three pulses are used. The first two must be of amplitude $H' > \Delta H$ and of duration τ to accomplish a $\pi/2$ rotation of the spins. The spacing Δt must be less than homogeneous T_2. Now a third pulse can be applied at a time Δt after the second pulse to produce an echo at a time Δt after the third

pulse. Δ t' can be much longer than homogeneous T_2. Hahn shows that this type of echo is possible because the transverse orientation of a spin at the time t is converted to the corresponding orientation with respect to the z-axis by the second pulse. This orientation can be preserved for a time T_1. When a third identical pulse is applied, the spins receive a transverse orientation which is similar to the orientation they receive after the second pulse in spin-echoes of the first type. An echo appears in a time Δt after the third pulse. This type of spin-echo is termed stimulated spin-echo. They should appear as long as $\Delta t' < T_1$. T_1 is measured by lengthening $\Delta t'$ until the echo disappears.

This method has a number of weaknesses in spite of the elaborate instrumentation it requires. The biggest of the weaknesses is that it does not measure T_1 as predicted by simple theory. The reason is cross-relaxation. This is an exchange of energy (or a mutual spin-flip) between spins which do not possess the same Zeeman energy. The characteristic time T_{12} associated with this relaxation is always less than T_1. In stimulated spin-echoes, the effect of cross-relaxation is to scramble the spins with different orientations with respect to the z-axis. This destroys the relation between the z-component of the spin orientation and the Larmor frequency. Thus, the spin-echo is destroyed in a time T_{12}. As long as any inhomogeneous broadening exists, cross-relaxation between different portions of the inhomogeneously broadened line is operative (also called spin diffusion). If a number of closely spaced energy levels exist, T_{12} can be very short. Yet, it is always longer than T_2. It can

THIS
PAGE
IS
MISSING
IN
ORIGINAL
DOCUMENT

1. T_2 is measured by the line width of the resonance.
2. T_2' (spin-spin or homogeneous relaxation time) is best measured by normal spin-echo.
3. T_2'' (inhomogeneous T_2) can be found by the relation $1/T_2 = 1/T_2' + 1/T''_2$.
4. T_{12} (cross relaxation time) is best measured by stimulated spin-echo.
5. No method of measurement of T_1 is particularly convincing. The simplest method is to use Bloch's steady-state saturation condition. The saturation-recovery method is very logical but not without practical difficulties. The large disagreement in T_1 measured in ruby by different workers does not encourage a great deal of confidence to be placed in any measurement. At liquid helium temperature (4.2°), the reported values of T_1 are .7 ms[51], 5 ms[52], 300 ms[53] and 25 ms[54]. There is also considerable disagreement over the temperature dependence of T_1[55]. Some, but by no means all of this discrepancy is due to the concentration dependence of T_1.

1.3 Microwave Source Frequency Stabilization

Two different sources were used at X-band at different times. The principal source was a Pound stabilized klystron designed and constructed by F. D. Clapp. In this system a small sample of the klystron output is taken by a directional coupler and fed into a "magic-T". The two side-arms of the "magic-T" are connected to a high Q, tunable reflection cavity and a crystal

modulator, respectively. A strong 30 mc signal modulates the impedance of the crystal so that the microwave reflected from the crystal is amplitude modulated at 30 mc. The detector arm detects the phaser difference between the reflection from the cavity and the modulated reflection from the crystal. The relation is shown in Fig. 4. If the phase and amplitude of the modulated reflection is adjusted as shown in the figure, the variation in the detected output is purely second harmonic when the klystron output frequency and the resonant frequency of the reflection cavity coincide. When the klystron frequency is too high, a 30 mc component of negative phase appears in the output. When the frequency is lower than the cavity frequency, a 30 mc component of the positive phase appears in the detector output. This output is amplified and converted into a d.c. error signal by a phase discriminator. The error signal is added in series with the klystron repeller voltage in such a phase as to constitute a negative feedback. The actual theory is more complicated because the modulated impedance of a crystal does not describe a straight line on the Smith chart. However, the adjustment of the stabilizer circuit is made by trial and error, so a precise theory is not necessary.

The tune-up procedure is described.

1. Frequency sweep the klystron. By adjustment of the klystron re-entrant cavity and the reflector voltage, locate the frequency at which stabilization is desired. This is usually the resonant frequency of the paramagnetic resonance cavity. It is located by observing the sharp dip in the reflection from the cavity

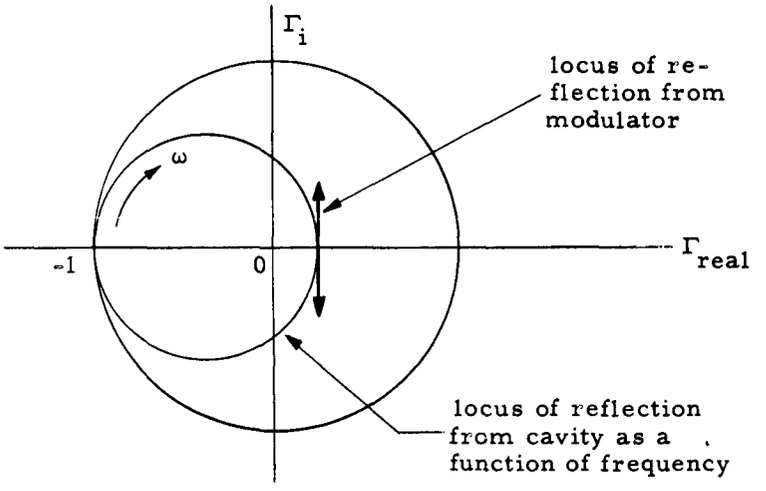

Relation between reflection from cavity and reflection from crystal modulator when stabilizer is properly tuned

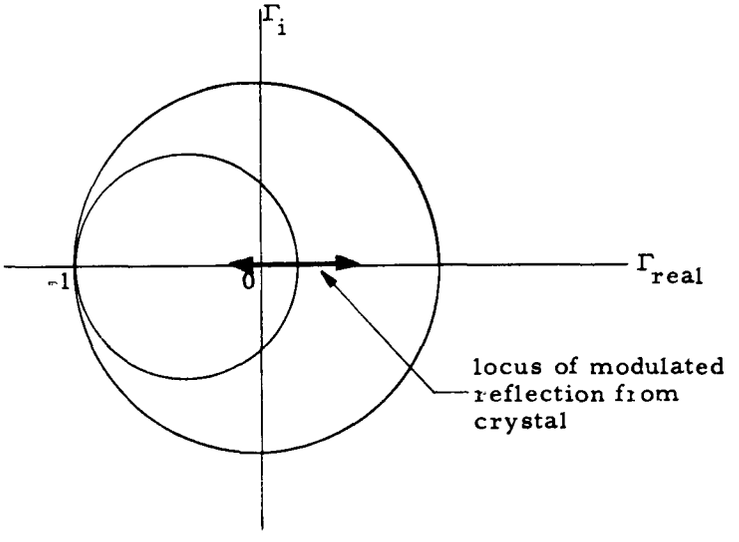

Improperly tuned stabilizer

Figure 4

displayed on the oscilloscope (Fig. 5).

2. Close the Pound stabilization feedback loop. Tune the reference cavity until an indication is seen in the neighborhood of the proper frequency (Fig. 6).

3. Adjust the 30 mc reference phase-shifter until the effect is maximized. It should put a "flat" on a portion of the klystron output, indicating constant frequency.

4. Adjust the reference cavity so that the "flat" coincides with the cavity resonance frequency. The result should look as in Fig. 7.

5. Adjust the tuner and phase-shifter in series with the modulation crystal to obtain the best flat. Care should be taken to avoid sharp trailing or leading spikes at the ends of the "flat" zone. This is a sign of potential instability and should be avoided, even at the cost of some flatness and width of the "flat" zone. Reduce 30 mc gain if necessary.

6. Gradually reduce the klystron sweep. As this is done, the duty rate on the klystron is changed from approximately 50% during full sweep to unity at no sweep. The change in average d.c. current detunes the klystron thermally. A fairly large adjustment in the klystron tuning is required to return the klystron to optimum operation as the sweep is reduced.

7. After the sweep has been reduced to zero, adjust the reference cavity again to make it coincident with the paramagnetic resonance cavity. This is done most accurately by a d.c. oscilloscope or a sensitive d.c. meter monitoring the reflection from the cavity. A minimum indication corresponds to proper adjustment.

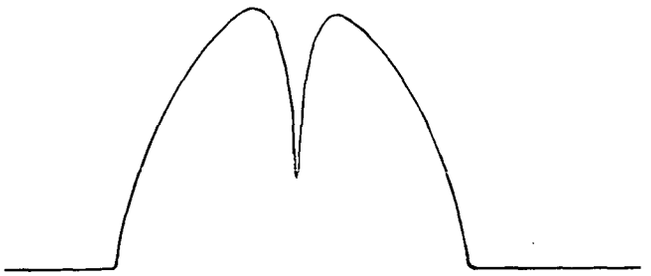

Figure 5. Klystron mode with cavity absorption

Figure 6. Initial indication of regulation

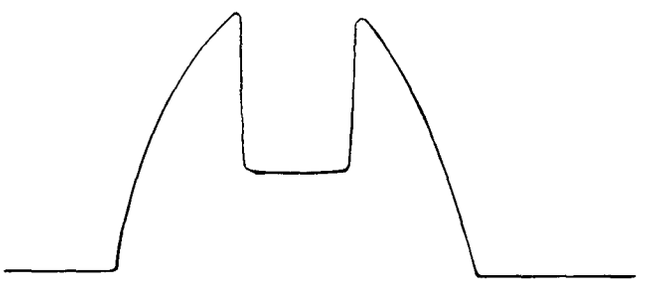

Figure 7. Regulation optimized on cavity frequency

The same procedure can be used for any frequency by using a wave-meter as a marker. The system is limited in range by the bandwidth of the components in the stabilizer circuit and by the tuning range of the reference cavity. This tuning range was 8.5 to 9.6 gHc for the stabilizer used.

With proper adjustment, the stability of this system is superior to the other systems used. Experience shows three factors to be important in the proper operation of this circuit.

1. The crystal holders for the 30 mc modulator and detector should be of the special modulator type. Normal audio output-type detector holders will filter out much of the 30 mc.
2. The crystal used in modulation and, particularly, detection of 30 mc must be carefully selected. It is found that the low cost 1N21B and 1N23 obtainable on surplus tend to be superior to the expensive low-noise crystals such as 1N23D, 1N23E, 418 and 408. The 30 mc output can easily vary 10 to 20 db between a selected crystal and a crystal picked at random.
3. The 30 mc signal generator must be free of second harmonics. Otherwise, an error signal will be fed to the klystron, even when the output frequency is in exact coincidence with the reference cavity.

The power supply was an FXR 819B regulated klystron supply. The klystron was a Raytheon 2k39 with an output power of about 500 mw. A regulated d.c. filament supply was added for additional stability.

A commercial stabilized oscillator LFE Model 814-X-21 was also used for a short time. This oscillator is stabilized by a large dual-mode reference cavity. The two modes are the orthogonal modes in an almost square cavity. The two resonant frequencies are almost, but not quite, degenerate. The klystron output excites both modes; crystals detect the excitation of each mode. The difference in the detected excitation is amplified and fed back to the klystron repeller in such a way as to keep the difference at a minimum. This keeps the klystron output frequency exactly midway between the two resonant frequencies of the reference cavity if the detectors are matched. A mismatch in the detector merely shifts the stabilization point closer to the cavity with the weaker detector. The stability of the unit seemed to be very good. The ease of tuning was its big virtue.

The third microwave source employed was a Varian V-153 klystron and an FXR 815 power supply. The frequency regulation was provided by a transistorized regulator designed by A. George.[56]

In this scheme, the total output of the klystron is slightly frequency-modulated at 60 kc. The paramagnetic resonance cavity itself acts as a reference cavity. When the klystron output is exactly resonant with the cavity, the reflection from the cavity is amplitude-modulated at 120 kc. When the frequency is off resonance, a 60 kc component appears. The phase is positive or negative depending on whether the frequency is higher or lower than the cavity resonance frequency. The 60 kc modulation is amplified and detected by a transistorized

phase-detector and d.c. amplifier. This error signal is fed back to the klystron reflector to correct the frequency.

The advantages of this system are:

1. Simplicity.
2. It can be used at any frequency. It will work equally well with S-band or k-band because it does not incorporate with any microwave network.
3. It locks on the actual experimental cavity and is, thereby, able to follow any drift in the resonant frequency.

The weaknesses are:

1. The klystron output is frequency-modulated. For high Q cavities, this modulation is very small and of no consequence. For low Q cavities, the modulation must be large to give adequate loop gain and may give trouble for narrow lines.
2. The gain of the loop is dependent on the microwave power level, crystal detector bias and cavity match.

The k-band source consisted of a Raytheon 2k33A or a 5645 klystron and an FXR 819 power supply. Regulation was provided by the FM modulation system described above. The maximum power output of the klystron is between 20 and 40 mw.

1.4 The Cavity

The construction and assembly of the cavity system is given in Fig. 8. The system consists of the input waveguide which is terminated in a slotted round flange, a silverplated copper

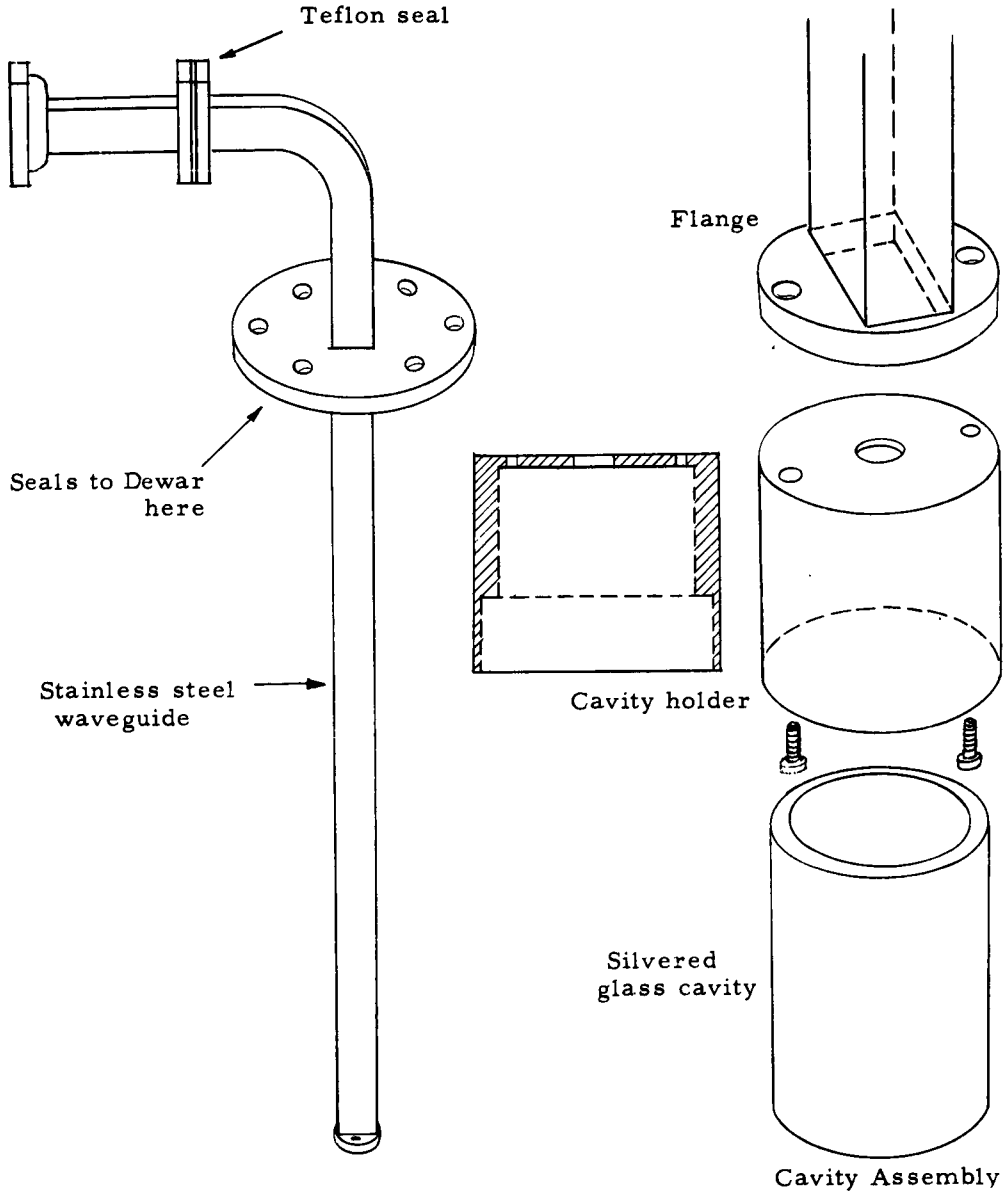
Teflon seal
Flange
Seals to Dewar here
Stainless steel waveguide
Cavity holder
Silvered glass cavity
Cavity Assembly

Figure 8

cavity-holder which is attached to the flange by means of two screws, and the silver-coated cylindrical glass cavity. The glass cavity is formed from standard pyrex tubing. The open end is ground flat on a grinding wheel. It is then sprayed with DuPont 4775 silver paint and baked at 550°C. This forms a very tough silver surface. The resistivity is appreciably higher than pure metallic copper. However, Q's in the neighborhood of 10,000 can be obtained. The glass cavity was necessary to allow penetration of the 100 kc magnetic field modulation into the cavity. The cavity is held in place by adhesive tape. The cavity-holder actually forms a portion of the TE_{112} cavity. The joint between the holder and the cavity is designed to be 1/4 wavelength away from the coupling end at 9 kmc. Several cavity-holders with coupling holes of different diameters were made. The holder with the best coupling was used for each experiment.

The cavity is enclosed in a double Dewar system. The interior of the second Dewar, including the cavity and waveguide, is sealed off from the outer atmosphere by means of a rubber gasget at the top of the Dewar and a teflon seal at the top of the waveguide. This prevents the continuous condensation of oxygen and water within the Dewar and cavity. The outer Dewar is exposed to atmosphere. It is filled with liquid N_2 when low temperature measurements are made.

The k-band cavity assembly is similar to the x-band assembly. It is illustrated in Fig. 9. In this case, only the coupling disk is changed for coupling adjustment instead of the

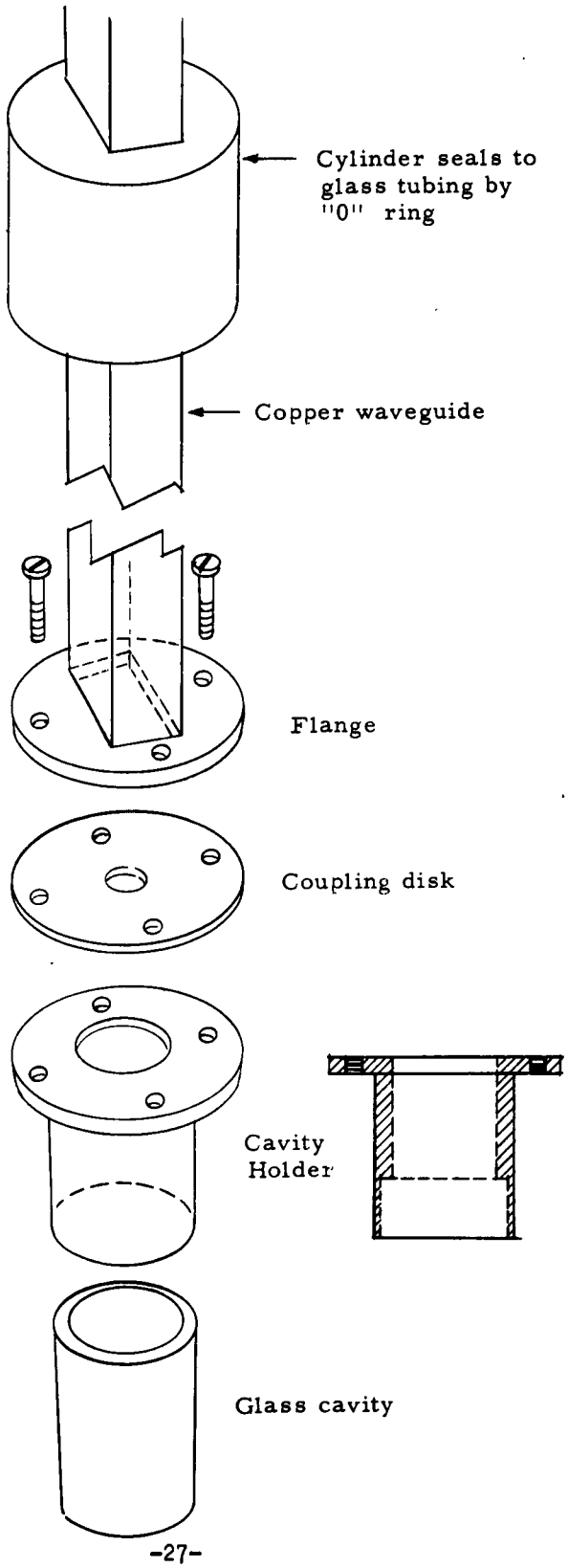
Cylinder seals to glass tubing by "0" ring
Copper waveguide
Flange
Coupling disk
Cavity Holder
Glass cavity

Figure 9

entire cavity-holder. At the magnet gap-width required at k-band, there is no room for an inner Dewar. Consequently, no liquid helium work can be done. The cavity is sealed off from liquid N_2 and from the atmosphere by a teflon seal at the top of the input waveguide and a narrow glass tube which is sealed to the waveguide by an "O"-ring. This assembly is then immersed in liquid N_2 contained in a Dewar of O.D. = 1 5/8". The maximum field attainable at this magnet-gap width is 7450 g, somewhat short of the value required for a free-spin resonance.

1.5 The Detection System

The detection crystal is mounted in a tunable mount. The crystal current is adjusted to approximately .05 ma by means of the bucking arm on the "magic-T". This is done by a variable attenuator terminated by a movable short. The phase of the bucking reflection is determined by the movable short. The amplitude is determined by the attenuator. For detection of absorption, the phase of the reflection from the bucking arm must be either in phase or 180° out of phase with the cavity reflection Γ_0. This is accomplished by adjusting the short position to give a maximum or minimum d.c. output from the crystal at a particular setting of the attenuator. The attenuator adds a small phase shift.

The 100 kc amplifier has a very narrow pass-band ($<$2kc) and a voltage gain of 1500. This is followed by a Tektronix 121 wide-band variable-gain amplifier with a maximum gain of 100. The wide bandwidth was not desirable, but the

calibrated variable gain was useful. The synchronous phase-detector is a standard circuit using 4 diodes (Fig. 10). The integration time was usually .01 s. At times longer integration times were used. The output of the synchronous detector is recorded by a Varian V-10 recorder with a maximum sensitivity of 5 mv f.s.

1.6 The Magnet

The magnet is an almost exact copy of the Varian V-4007 6" magnet with a rotating but not tilting base. The power supply is a Varian 2200c Magnet Supply. The combination of this magnet and supply provides a maximum field of 5500 gauss at standard magnet gap and up to 10,000 gauss with special pole inserts installed. The current (field) can be swept slowly by an electrical sweep signal or by the manual control on the front panel over limited ranges. By using the step-range switch and the electrical or manual sweep, the entire magnetic field range from 0 to maximum field can be covered. The electrical sweep is very non-linear, the field increment for a given sweep signal increment being roughly proportional to the value of the field. The manual sweep rate is less variable from range to range but very non-linear within each range. The sweep is very slow at the beginning of each range and very fast at the end of each range. These non-linearities contribute to the inaccuracy of line width measurements. The current was also swept mechanically by driving the manual control knob with a synchronous motor with drive belt.

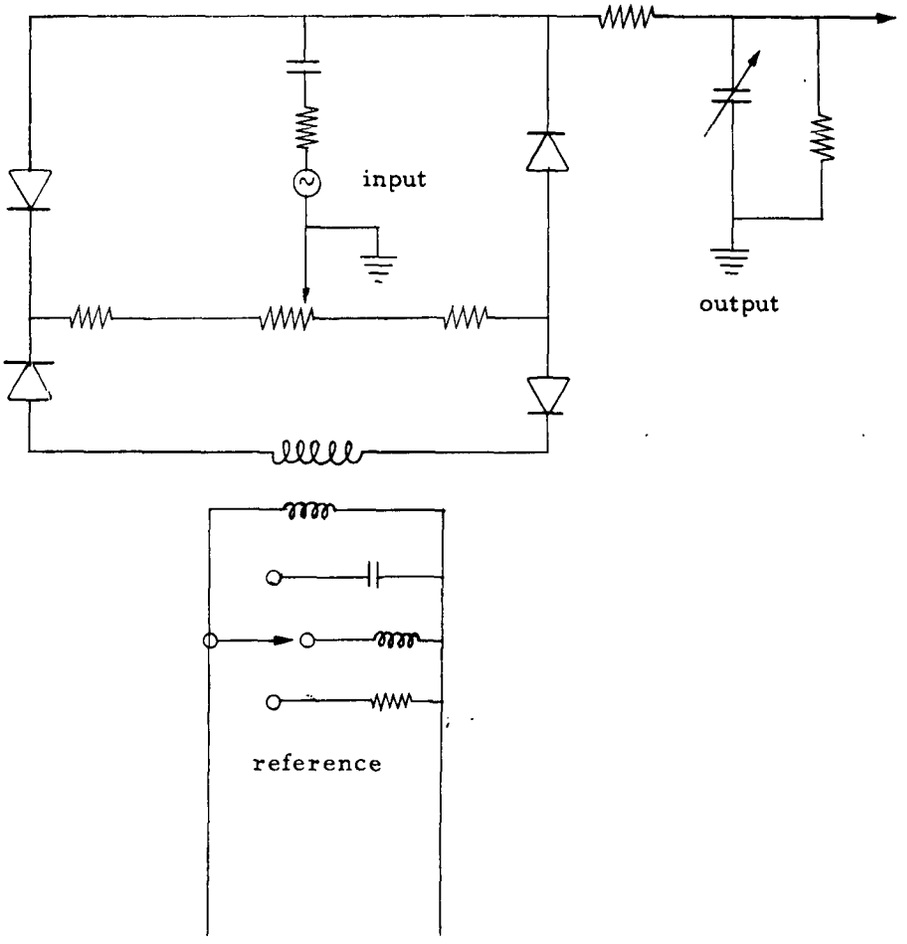

Figure 10

The magnetic field is determined by observing the magnet current and referring to a calibration chart. The calibration was made by a Sensitive Research Instrument Corp. Model FM flip coil and flux meter. It was double-checked by nuclear magnet resonance in the neighborhood of 3000 gauss. The measurements are always made with the current going up monotonically from 0. The measurements are accurate to about 10 gauss.

1.7 Field Modulation

The field modulation is provided by a modulation coil of 200 turns of No. 30 wire in 4 coils of 50 turns each. The coils are connected as in Fig. 11 to reduce the stray electric field to a minimum. The modulation signal is provided by a HP-200-C oscillator and a power amplifier which gives a maximum output voltage of 70 volts r.m.s. at 100kc.

The modulation was measured inserting a small pickup coil in the cavity and measuring the open-circuit induced voltage. It shows the maximum modulation field to be 1 gauss peak to peak.

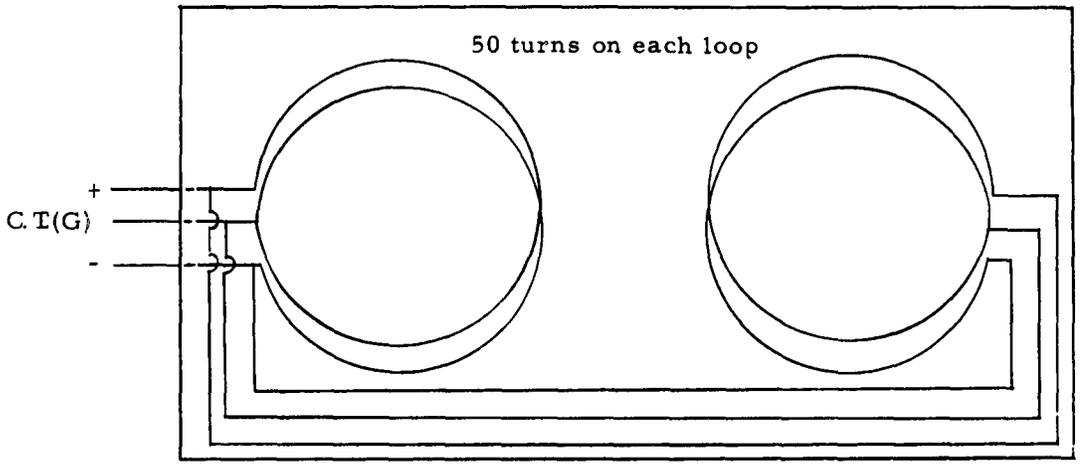

Coils are mounted on card board which is wrapped around Dewar.

Figure 11. Modulation coil

CHAPTER 2

PARAMAGNETIC RESONANCE IN $CaCO_3$ (CALCITE)

2.1 The Crystal Structure of Calcite

The crystal structure of calcite is described by Bragg[44] and Wyckoff.[48] The structure is rhombohedral with the space group symmetry $R\bar{3}c$. There are two molecules in a unit cell. The position of the ions are given by Wyckoff as:

Ca: (b) 1/4, 1/4, 1/4; 3/4, 3/4, 3/4

C : (a) 0, 0, 0; 1/2, 1/2, 1/2

O : (e) $u, \bar{u}, 0; \bar{u}, 0, u; 0, u, \bar{u};$

$\frac{1}{2}-u, u+\frac{1}{2}, \frac{1}{2}; u+\frac{1}{2}, \frac{1}{2}, \frac{1}{2}-u; \frac{1}{2}, \frac{1}{2}-u, u+\frac{1}{2}$

The parameters are $A_o = 6.361\text{A}$, $\alpha = 46°6'$, $u = .243$. The structure is illustrated in Figs. 12 and 13.

Each Ca^{2+} ion is surrounded by six CO_3 groups from neighboring cells. They form an equilateral triangle above the Ca^{2+} ion and another equilateral triangle at the same distance below the ion. The three CO_3 above the Ca^{2+} are related by inversion to the lower ones as required by the inversion symmetry of the site.

The positions of the CO_3 groups about the two Ca^{2+} ions are not identical. They take positions and orientations in the two sites which are related by a reflection across a vertical reflection plane which includes one of the rhombohedral vectors. The six CO_3 groups each contribute one oxygen to form an approximately octahedral arrangement of six O^{2-} ions about the Ca^{2+} ion.

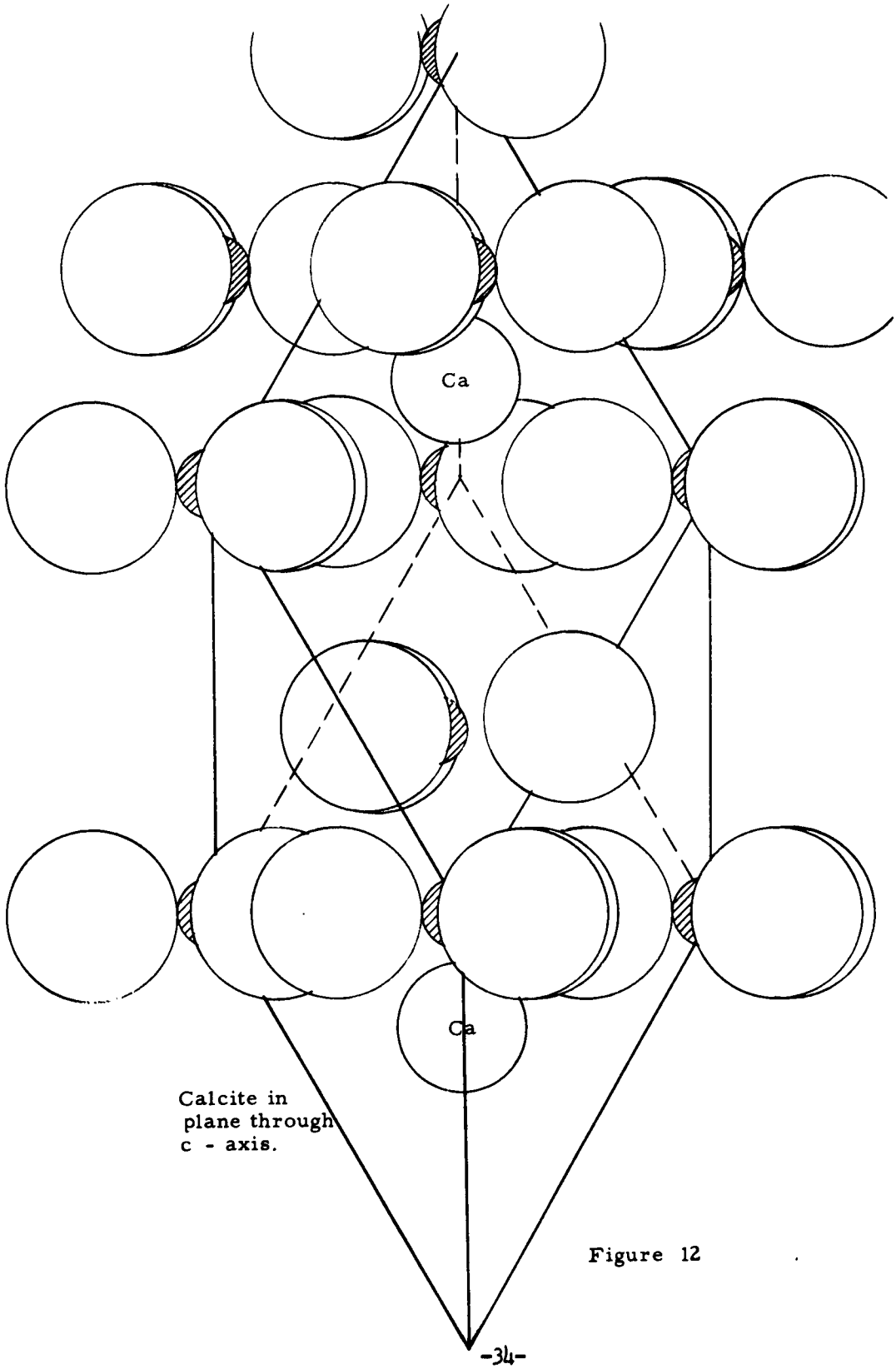

Calcite in plane through c - axis.

Figure 12

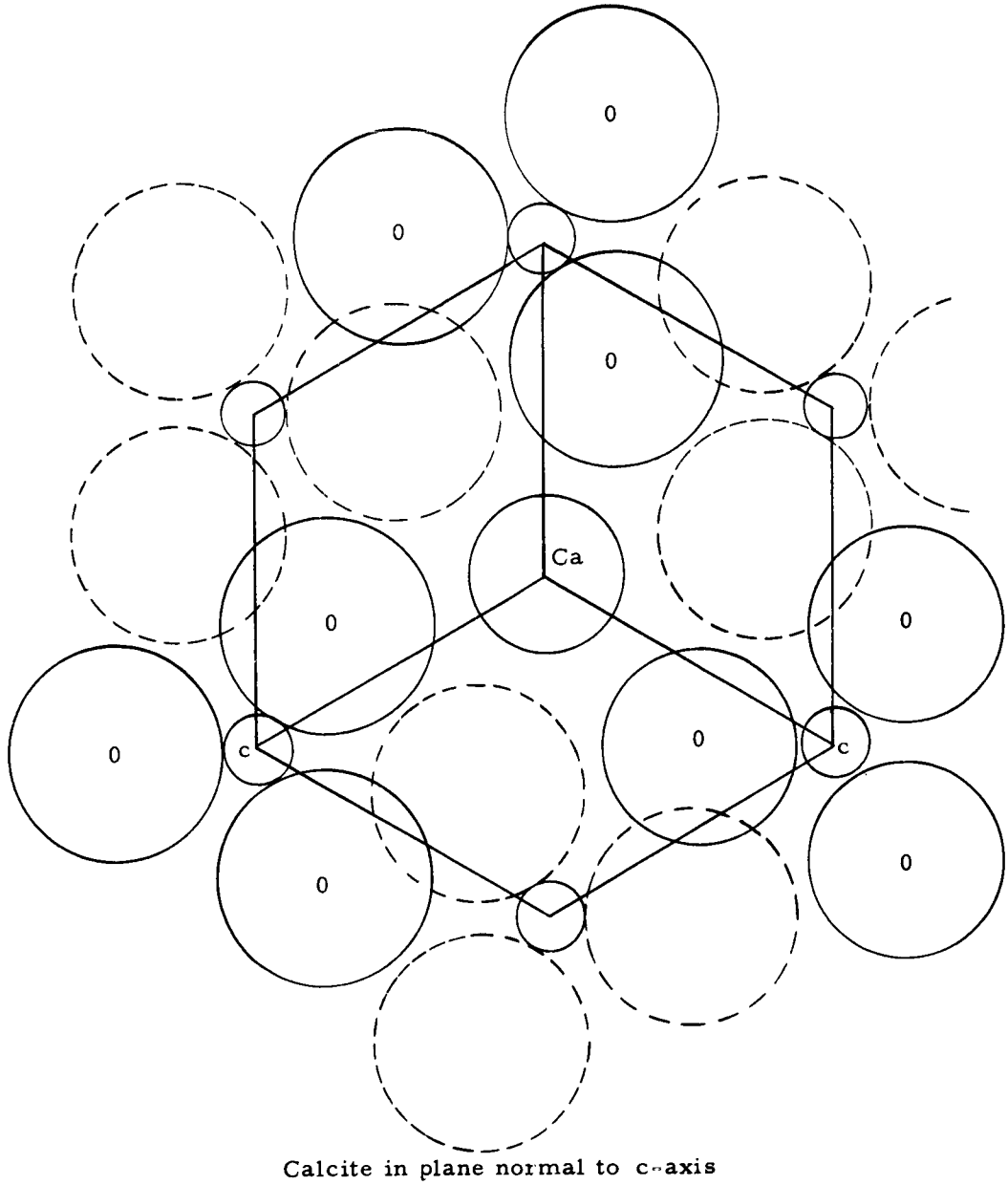

Calcite in plane normal to c-axis
Dotted circles show Oxygens in a plane $\frac{c}{3}$ below

Figure 13

These relations are lucidly illustrated by Kikuchi.[57] His figures are reproduced in Fig. 14.

Calcite displays particularly perfect cleavage planes. The cleavage $\{10\bar{1}1\}$ is perfect. This gives crystals of calcite a rhombohedral external form which possesses the same C-axis as the true unit cell, but compressed along the C-axis. A typical cleavage rhombohedral is shown in Fig. 15. The normal to the cleavage planes is parallel to the plane which reflects one type of Ca^{2+} site into the other type.

A sharp tool and a tap of a hammer will produce clean cleavage surfaces by which the crystal can be accurately oriented.

2.2 The Crystalline Field of Calcite

In order to estimate the nature of the spectrum of a paramagnetic ion substituting in the Ca^{2+} site, a calculation of the crystalline field is made. This is done in a crude fashion by replacing each ion in the crystal by a point with the same charge as its valence. When the field is expanded in spherical harmonics the relevant portions of the field are the terms of even ℓ. For the symmetry $\bar{3}$, the form of the relevant field is

$$V = A_2^0 Y_2^0 + A_4^0 Y_4^0 + A_4^3 \left[Y_4^3 + Y_4^{-3} \right]$$

The total field is the sum of the fields due to all the ions in the lattice. The calculation is somewhat similar to the calculation of lattice energy, but it is much more involved. In the lattice energy calculation, the potential sought is the sum of

Figure 14

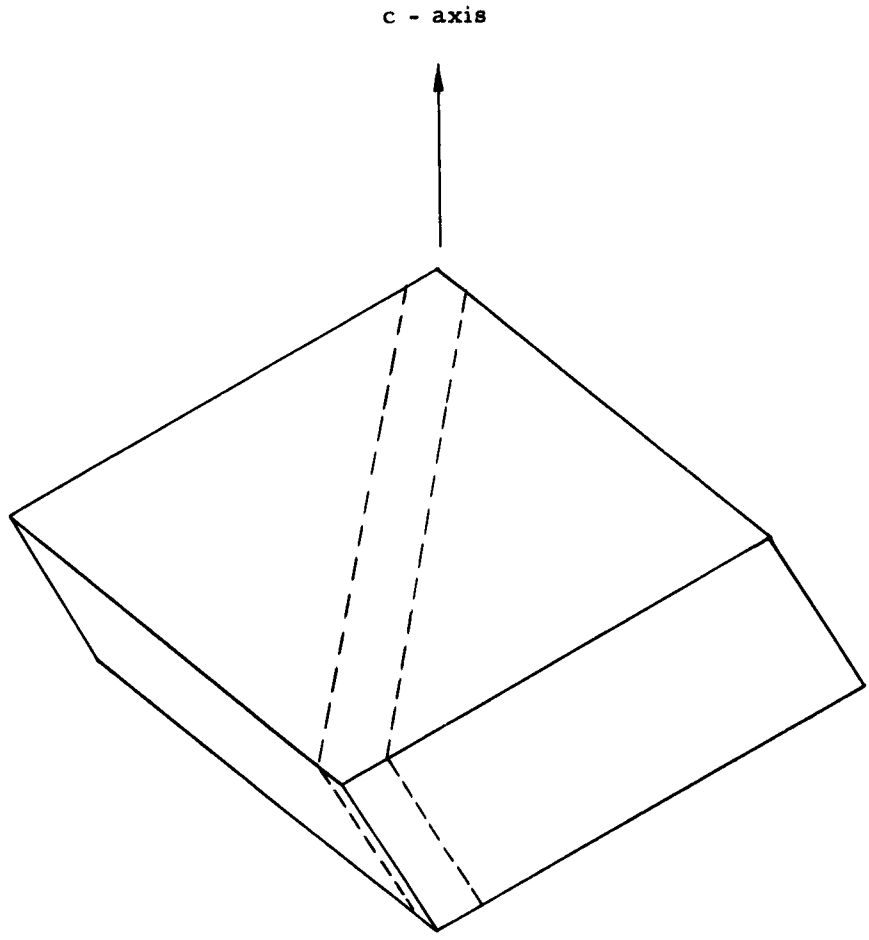

A cleavage rhombohedron of calcite.
One sample was cut along the dotted lines.

Figure 15

the mono-pole potentials due to each ion. First of all, the contribution due to an ion is only a function of its charge and distance from the origin and not of its angular position. The convergence of the sum is very rapid when shells of ions approximately equidistant from the origin are taken in such a way that the net charge of the shell is zero.[58] In the second place, an average position of the net charge for each ion gives the correct potential. A non-isotropic distribution of electrons about the neighboring ions will not change the result. We know that the calculated lattice energies are very close to measured values.[59]

In the potential calculation required here, the angular position of the ion with respect to the origin strongly influences the contribution which the ion will make to a particular term in the expansion. Therefore, taking shells of neutral charge will not help convergence very much. Furthermore, for the calculations of terms of $\ell = 2$ and 4, replacement of the nearest neighbors by point charges at the ion centers is not as good an approach. Co-valent bonding of the central ion to its neighbors can modify the potential.

Nevertheless, this type of calculation is not altogether valueless. It can certainly determine the sign of the cubic field. It can also give some idea of the relative strength of the field. Baker et al.[60] has found that such calculated field-strengths are able to account for the zero-field splittings of Mn^{2+} in cubic fields.

The simplest way to compute the field is to express the field due to each ion as a series of axial harmonics with the axis z' along the line joining the ion to the origin. They are

then converted to spherical harmonics whose z-axis is along the crystalline C-axis by using biaxial harmonics.[61] This procedure gives the following expression for the coefficients A_ℓ^m:

$$A_\ell^m = \frac{4\pi\,\ell}{2\ell+1}\, r^\ell \sum_i \frac{Z_i}{R_i^{\ell+1}}\; Y_\ell^m(\Theta_i \Phi_i)$$

Here, Z_i is the valence of the i^{th} ion and Φ_i and Θ_i are the spherical coordinates of the i^{th} ion when the z-axis of the coordinate system is the C-axis.

The high symmetry of the site also simplifies the calculations. The symmetry $\bar{3}$ means that neighbors can be grouped into sets of six ions which all make the same contribution. The exceptions are ions on the axis which can only be paired off by the inversion symmetry of the site.

The crystalline field of calcite about the Ca^{2+} site was calculated by taking the eight nearest CO_3^{2-} groups and the eight nearest Ca^{2+} ions for charge neutrality. The result was

$$A_2^0 = \ell\sqrt{\frac{4\pi}{5}}\, r^2(-.0132)$$

$$A_4^0 = \frac{24\pi\ell}{9}\sqrt{\frac{9}{4\pi}}\cdot\frac{1}{8}\, r^4(+.3855)$$

$$A_4^3 = \frac{24\pi\,\ell}{9}\,\frac{105}{8\sqrt{35\pi}}\, r^4(.0328)\,\ell^{i3\phi}$$

where ϕ is $23^\circ 33'$ clockwise from the nearest oxygen.

In making this calculation, three observations are made.

1. All the ions included in the calculation make

significant contributions to A_2^o.

2. The mutual cancellation of the terms contributing to A_2^o is almost perfect. Therefore, the value and sign are completely unreliable except to indicate that the term is small.

3. A_4^o and A_4^3 are determined approximately by the six nearest neighbor oxygens. This is due to the factor $\frac{1}{R_1^5}$.

It is interesting to compare this result with the field of six O^{2-} in a perfect octahedron. In this case A_2^o vanishes and

$$\frac{A_4^o}{A_4^3} = \left(\frac{7}{10}\right)^{\frac{1}{2}} = .836$$

In calcite this ratio is .994.

A comparison with ruby (corundum) is also interesting. A similar calculation in ruby gave

$$A_2^o = \ell\sqrt{\frac{4\pi}{5}}\, r^2(.196)$$

$$A_4^o = \frac{3\ell}{4}\sqrt{\frac{4\pi}{9}}\, r^4(1.24)$$

$$A_4^3 = \frac{24\ell}{9}\,\frac{105}{\sqrt{35\pi}}\cdot\frac{1}{8}\, r^4(.0457)$$

The smaller size of Al^{3+} places the O^{2-} closer to it, and the field is correspondingly stronger. Cancellation is again high in A_2^o so that its value is not reliable.

$$\frac{A_4^o}{A_4^3} = .76$$

Optical measurements show that the crystalline field of ruby is so close to cubic that the effect of the deviation from cubic is smaller than the line width and cannot be measured. This is not so surprising. If Al_2O_3 were a purely ionic crystal, it is very reasonable to expect the large O^{2-} to form a nearly perfect octahedron around the Al^{3+}. Actually, the bond between Al^{3+} and the O^{2-} may not be purely ionic.[45]

In the case of calcite, the CO_3 group is definitely known to be non-ionic.[45] The grouping of CO_3 is much more rigid than the bond between Ca^{2+} and O^{2-}. Furthermore, Ca^{2+} is a relatively large ion. Therefore, less regularity in the coordination about Ca^{2+} can be expected. The calculations, however, do not show a decisive difference.

2.3 The Spectra of Paramagnetic Ions in Calcite - Review of Theory

The paramagnetic ions which would give interesting spectra in calcite are Fe^{3+}, Gd^{3+}, Cr^{3+}, Cr^{2+} and Ni^{2+}. The spectrum expected of each ion will be discussed here.

Fe^{3+}

The ionic state under Russel-Saunders coupling is given by L = 0, S = 5/2. The orbital state is a singlet. Therefore, the orbital state in a crystalline field is also a very pure singlet. The spin-Hamiltonian must have a form which is consistent with the crystalline field symmetry. For a crystalline field of trigonal symmetry, it is given by Bleaney and Trenham.[62]

$$\mathcal{H}_s = g\beta \bar{H}\cdot\bar{S} + DS_z^2 + \frac{1}{6}a(S_{x'}^4 + S_{y'}^4 + S_{z'}^4) + \frac{7F}{36}\left(S_z^4 - \frac{95}{14}S_z^2\right) \tag{2.1}$$

z is the C-axis of the crystal, and x', y' and z' are cubic axes in which the z-axis would be in the (111) direction. In terms of the trigonal axis

$$\mathcal{H}_s = g\beta \bar{H}\cdot\bar{S} + DS_z^2 + \frac{7}{36}(-a+F)\left(S_z^4 - \frac{95}{14}S_z^2\right) - \frac{\sqrt{50}a}{180}\left\{S_z(S_+^3 + S_-^3) + (S_+^3 + S_-^3)S_z\right\} \tag{2.2}$$

The g-value for Fe^{3+} is always very close to 2 and can be regarded as isotropic. The energy levels at zero field are

$$E_1 = \frac{13D}{4} - \frac{1}{2}(a - F) \pm \frac{1}{6}\sqrt{(18D + a-F)^2 + 80a^2}$$

$$E_2 = \frac{9D}{4} + (a-F)$$

The energy as a function of magnetic field when D is large is given by Prokhorov and Kornienko[63] for $H_o \| C$

$$M = \pm\frac{5}{2} \leftrightarrow \pm\frac{3}{2} : g\beta H_{1,5} = hf \pm \left\{4D - \frac{4}{3}(a-F)\right\} - \frac{20}{27}\frac{a^2}{g\beta H_{1,5} - 2D}$$

$$M = \pm\frac{3}{2} \leftrightarrow \pm\frac{1}{2} : g\beta H_{1,2} = hf \pm \left\{2D + \frac{5}{3}(a-F)\right\} + \frac{20}{27}\frac{a^2}{g\beta H_{1,4} + 2D}$$

$$M = +\frac{1}{2} \leftrightarrow -\frac{1}{2} : g\beta H_3 = hf - \frac{20}{27}a^2\left(\frac{1}{g\beta H_3 + 2D} + \frac{1}{g\beta H_3 - 2D}\right) \tag{2.3}$$

For $H_o \perp C$, we must assume that either $g\beta HS \ll DS_z^2$ or that $g\beta HS \gg DS_z^2$ to obtain expressions for the energies without the

use of a computer.

For $g\beta HS \ll DS_z^2$, the energy intervals are given by

$$hf = 4D - \frac{3g^2\beta^2H^2}{8D} - \frac{4}{3}(a-F) + \frac{10}{27}\frac{a^2}{D}$$

$$hf = 2D + \frac{5}{3}(a-F) + \frac{10a^2}{27D} + g^2\beta^2H^2\ \frac{11}{16D} \pm \frac{2}{\frac{3}{2}g\beta H \pm 2D}\ \pm \frac{3}{2}g\beta H \qquad (2.4)$$

The case where $g\beta \bar{H}\cdot\bar{S} \gg DS_z^2$ is given by Bleaney and Trenham.[42]

The approximate behavior of the energy levels as a function of the magnetic field at $\theta = 0$ is shown in Fig. 16. The spectrum as a function of field should show a symmetrical array of five lines, with the strongest center line at the free-spin resonance value.

The ϕ-variation of the spectrum is due entirely to the portion of the spin-Hamiltonian which is the spin-operator equivalent of Y_4^3. This function has a ϕ-variation of $P_4^3(\cos\theta)\cdot\sin 3\phi$. No ϕ variation is expected on the equator and at the poles where P_4^3 vanishes.

The two Fe^{3+} (Ca^{2+}) sites in calcite are non-equivalent because of the difference in their three-fold symmetries. For a general orientation, the spectra should differ by this difference. The two sites, however, are related by a reflection across a vertical reflection plane which includes a rhombohedral axis of the unit cell. The two spectra should coincide when the magnetic field is in this plane. Since there are three such planes, the coincidence should appear every 60 degrees in ϕ. Midway between

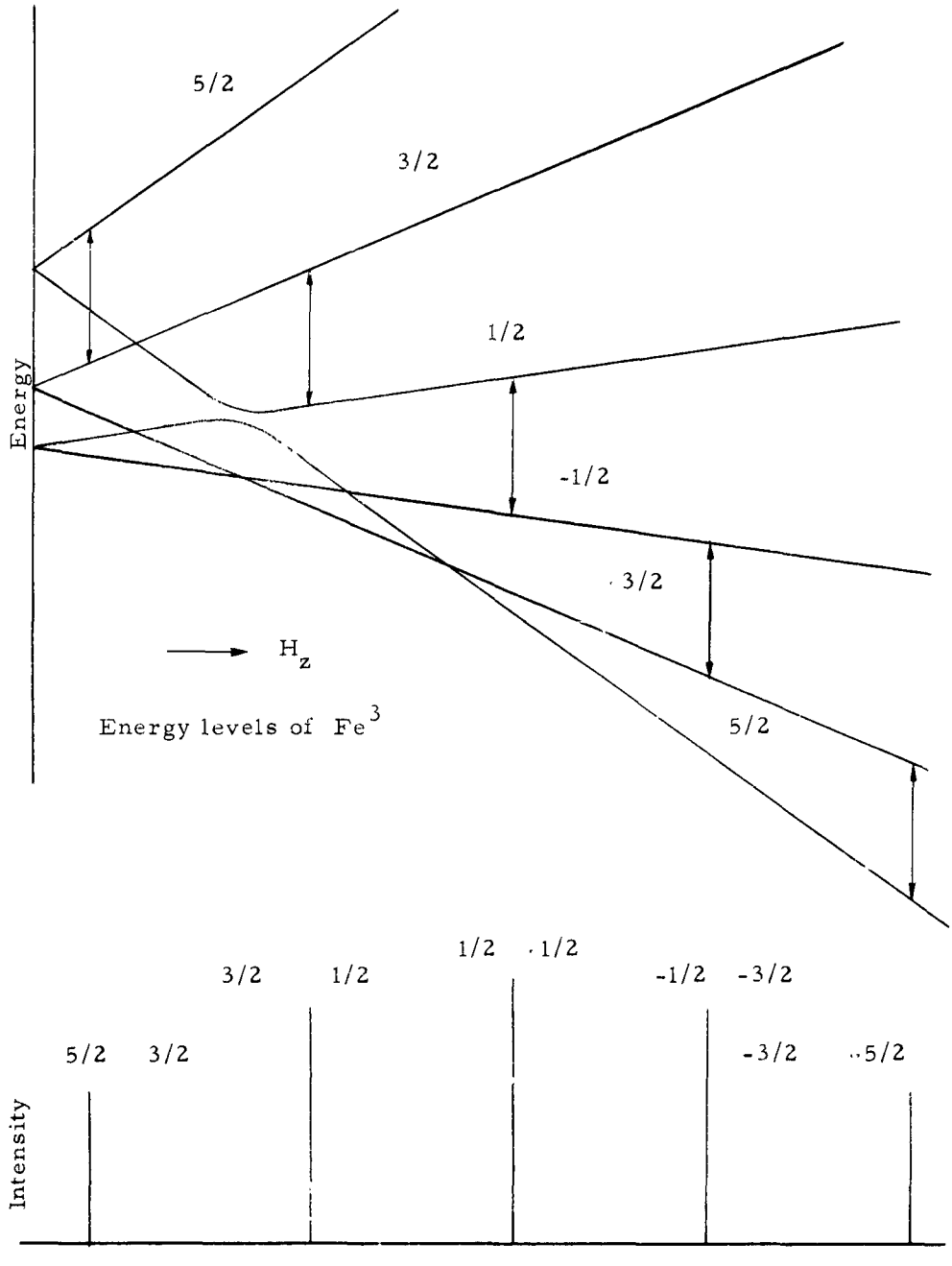

Spectrum of Fe^3

Figure 16

the points of coincidence, the spectra should show a maximum deviation.* The two spectra also coincide when $\theta = 0$ or $\theta = 90^{\circ}$.

Because Y_4^3 is an odd function of θ, the complete variation of the spectra as a function of θ can be obtained only by a measurement from 0 to 180°. In most other cases, the spectrum is even and only requires measurements from 0 to 90°.

Fe^{57} of 2% abundance possesses a nuclear spin of 1/2. It is very small, but it has been detected.[64]

The replacement of the divalent Ca^{2+} ion by a trivalent Fe^{3+} requires a compensation for the charge difference. This can take the form of a Na^{+} impurity in the neighborhood or a replacement of a CO_3^{2-} by BO_3^{3-}. If the compensation is sufficiently close to the iron site, it will alter the point symmetry from $\bar{3}$ to 1 (triclinic) unless the compensation takes place on the C-axis. This drastic change in symmetry should be very easy to detect because the spectra would exhibit characteristic features. When the compensation takes place on the C-axis, the point symmetry changes from $\bar{3}$ to 3. This change in symmetry adds an odd component to the crystalline field at the Fe^{3+} site. But,

*This is so because the variation is purely sin 3ϕ. For a general three-fold symmetry, the points of maximum deviation do not necessarily fall midway between the points of coincidence. This can be illustrated by superimposing two identical equilateral triangles, one rotated a small angle from the other. The reason for this difference in behavior lies in the presence of higher harmonics in the latter case.

the behavior of a paramagnetic ion is determined only by the even part of the field. Therefore, the form of the spin-Hamiltonian is unchanged by an axial compensation.

The same considerations apply to all trivalent ions such as Cr^{3+} and Gd^{3+}.

Cr^{3+}

The ionic state under Russel-Saunders coupling is $S = 3/2$, $L = 3$. In the octahedral field of calcite, the 7-fold orbital degeneracy is split into a lowest singlet and two upper triplets. The lowest singlet is separated from the other states by a large energy. Therefore, the orbital moment is very well quenched. This leads to a value of g very close to 2 and a long relaxation time T_1.

The spin-Hamiltonian of Cr^{3+} should have the same form as in ruby.

$$\mathcal{H}_s = g\beta\vec{H}\cdot\vec{S} + DS_z^2 \qquad (2.5)$$

The g-value is almost isotropic. To be exact, quartic terms are also expected by the symmetry. However, these terms have no matrix elements in the manifold of $S = 3/2$, so they can be omitted.

This Hamiltonian has axial symmetry -: no ϕ-variation is present. The energy levels in zero field are

$$m = \pm 3/2 \longrightarrow 9D/4$$
$$m = \pm 1/2 \longrightarrow D/4$$

The energies in a strong magnetic field are given by

$$E\left(\pm\frac{3}{2}\right) = \pm\frac{3}{2}g\beta H + \frac{D}{2}(3\cos^2\theta-1)\frac{9}{4} \pm \frac{3\sin^2\theta\cos^2\theta D^2}{g\beta H} \pm \frac{3D^2\sin^4\theta}{2g\beta H}$$

$$E\left(\pm\frac{1}{2}\right) = \pm\frac{1}{2}g\beta H + \frac{D}{2}(3\cos^2\theta-1)\frac{1}{4} \mp \frac{3D^2\sin^2\theta\cos^2\theta}{g\beta H}$$

$$\pm \frac{4D^2\sin^2\theta\cos^2\theta}{g\beta H} \pm \frac{3D^2\sin^4\theta}{2g\beta H} \qquad (2.6)$$

The energy differences between levels are $m = \pm 3/2 \leftrightarrow \pm 1/2$:

$$\Delta E = hf = \pm g\beta H + D(3\cos^2\theta-1) + \frac{D^2}{g\beta H}(2\sin^2\theta\cos^2\theta)$$

$$m = \frac{1}{2} \longleftrightarrow -\frac{1}{2}$$

$$E = hf = g\ H + \frac{2D^2}{g\beta H}\left\{-\sin^2\theta\cos^2\theta + \frac{3\sin^4\theta}{2}\right\}$$

The variation of energy levels with magnetic field for $H = H_z$ is given in Fig. 17. The spectrum consists of a symmetric array of three lines with an intensity ratio of $\sqrt{3}:2:\sqrt{3}$. The two ion sites are not distinguishable.

The θ-variation of the spectrum follows $Y_2^0 = 1/2(3\cos^2\theta - 1)$ to the first order. This means that the three resonance lines will collapse into one line at $\theta \sim 55^\circ$, for which $Y_2^0 = 0$.

Chromium has one odd isotope Cr^{53} with an abundance of 9.5%. The nuclear spin is 3/2. This splits the 9.5% into four equally spaced lines making the intensity of the hyperfine line approximately 1/40 of the center line. These lines have been observed in ruby and MgO. The splitting is small and difficult to identify when the lines are wide.

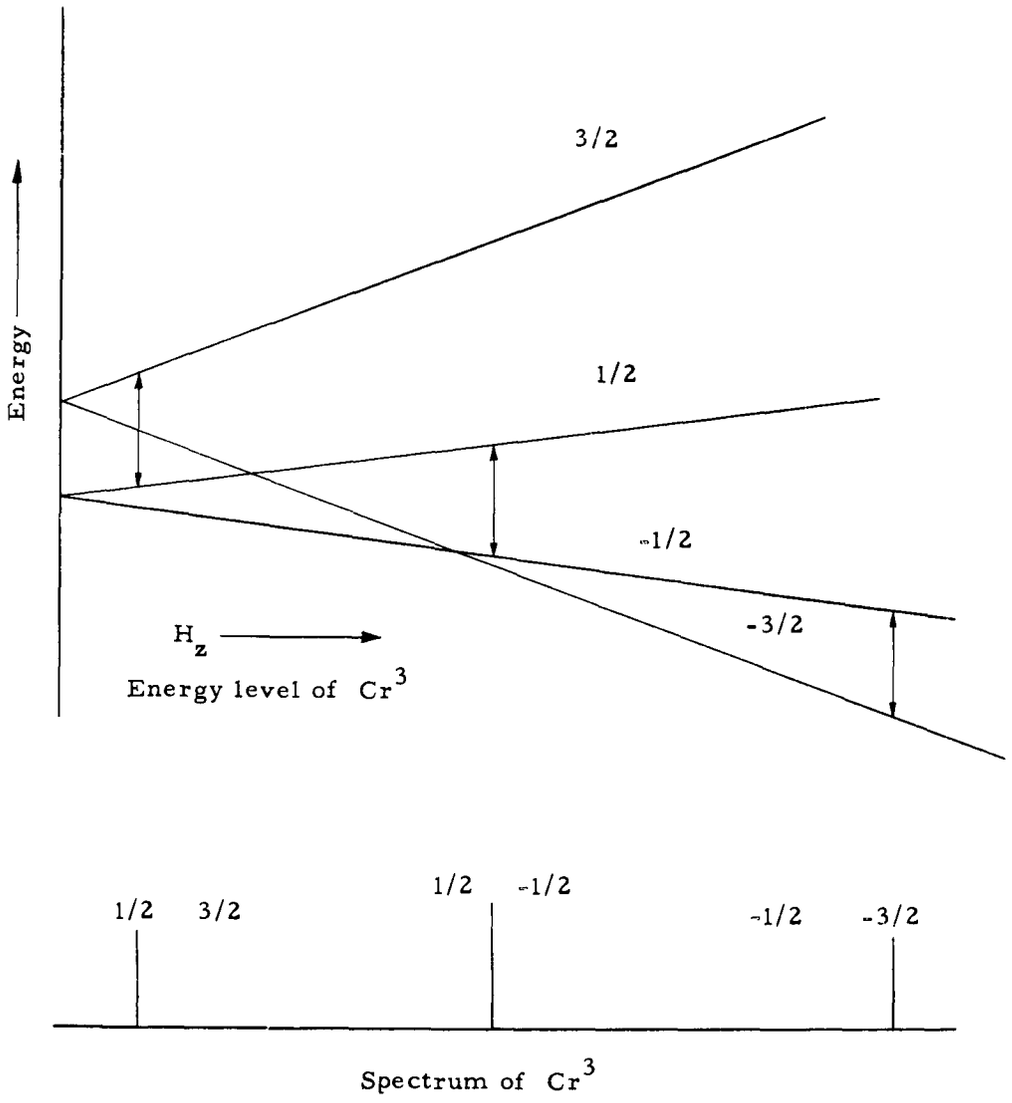
3/2
1/2
-1/2
-3/2
Energy
H_z
Energy level of Cr^3
1/2
3/2
1/2
-1/2
-1/2
-3/2
Spectrum of Cr^3

Figure 17

Ni^{2+}

The ionic state with Russel-Saunders coupling is S = 1, L = 3. The 7-fold orbital degeneracy is split by the crystalline field into two triplets and a lowest singlet. The separation of this level from the upper levels is similar to that in the case of Cr^{3+}. However, the "quenching" of the orbital moment is less complete due to the very strong spin-orbit coupling. The spin-orbit coupling constant for the free ion is $-355\ cm^{-1}$ in contrast to $+87\ cm^{-1}$ for Cr^{3+}. This results in a fairly large positive deviation of g from 2. The zero-field splitting is also large. The relaxation time is shorter than Cr^{3+}.

The spin-Hamiltonian is given by

$$\mathcal{H}_s = \beta H \cdot g S + D S_z^2$$

The quartic terms are omitted for the same reasons as in Cr^{3+}. g is usually almost isotropic. The energy levels in zero-field are

$$m = 0, \quad E = 0$$

$$m_s = 1, \quad E = D$$

The energy levels for all orientations of the magnetic field can be solved exactly in this case because there are only three spin states. For $H = H_z$ the energies are simply

$$m_s = 0 \quad E = 0$$

$$m_s = +1 \quad E = D + g H$$

$$m_s = -1 \quad E = D - g H$$

Only transitions from $m_s = 0$ to the other states is permitted. Only one of these transitions can be observed at a single

frequency. If D is large, no resonance is observed in the microwave region.

The odd isotope Ni^{61} has a nuclear moment of yet unknown value. The abundance is 1.25%. The hyperfine lines have never been observed.

The variation of energy levels with magnetic field is sketched for $H = H_z$ in Fig. 18.

Cr^{2+}

The ionic state with Russel-Saunders coupling is $S = 2$, $L = 2$. The five-fold orbital degeneracy is split by an octahedral field into a lower doublet and a higher triplet. The lower doublet is non-magnetic. When multiplied by the five-fold degeneracy of the spins, the ground state is ten-fold degenerate. Spin-orbit coupling splits this degeneracy into three doublets and three singlets.[18] A very rough calculation shows the splittings to be in the order of 1 cm^{-1}. However, transitions are almost completely forbidden between adjacent states.

The situation described is very unlikely. The orbital degeneracy is probably removed by the Jahn-Teller effect to produce a fluctuating orbital ground state whose average symmetry is either trigonal or axial. It is difficult to predict the spectrum by theory. In this case, theory must follow from experimental observations.

Figure 18

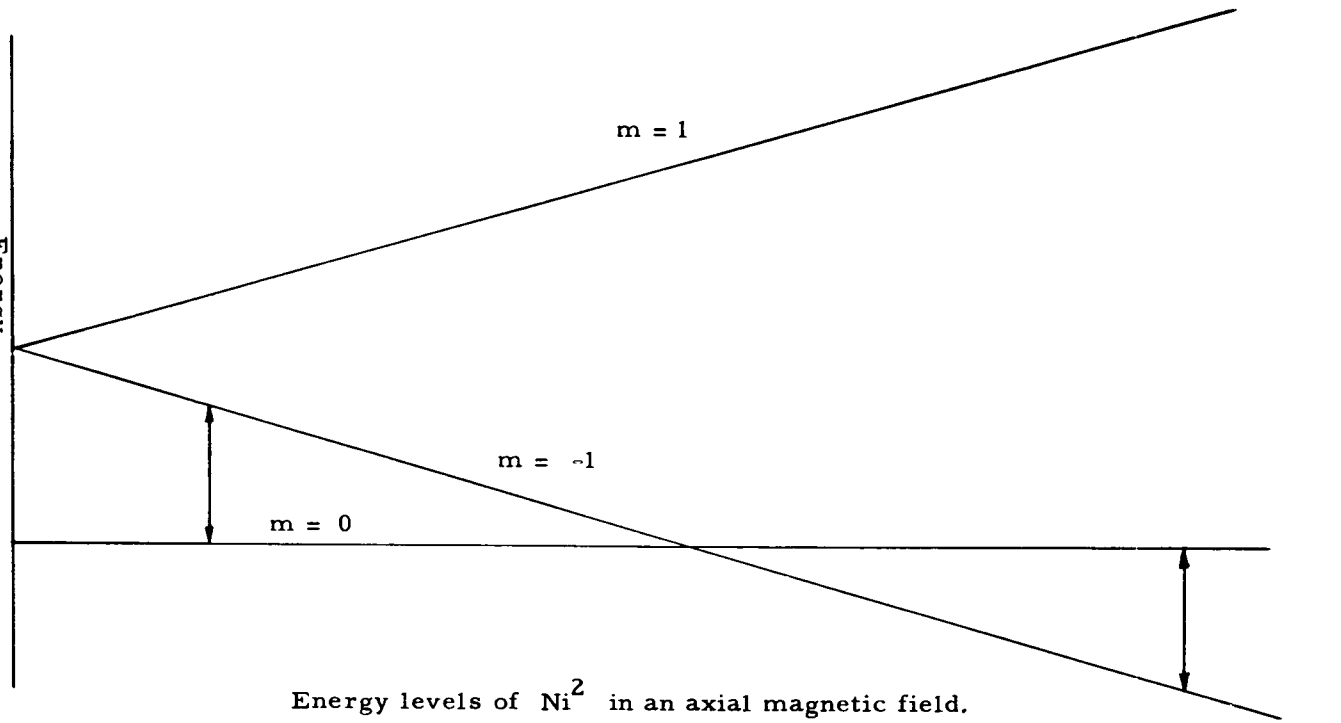

Energy levels of Ni^{2} in an axial magnetic field.

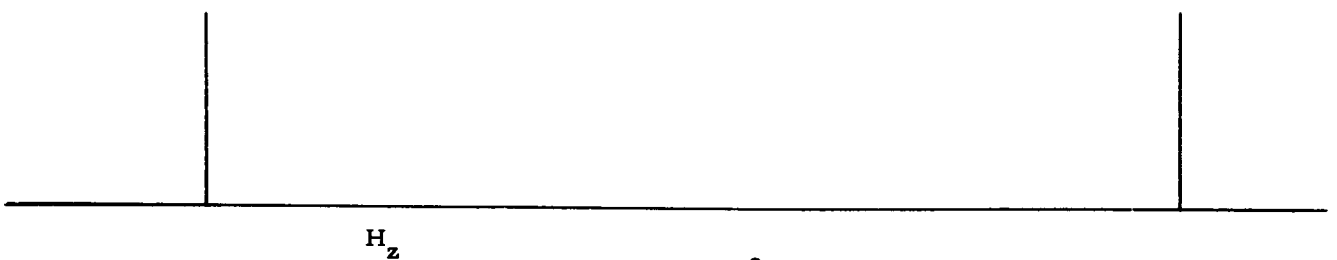

Spectrum of Ni^{2}

Gd^{3+}

The ionic state of Gd^{3+} with Russel-Saunders coupling is $S = 7/2$, $L = 0$. There is no spin-orbit coupling to the first order. The spin-Hamiltonian for the case does not follow from the theory for the iron group. The theory has been discussed by Judd,[65] Elliot and Stevens,[66] Hutchinson et al.[67] and Watanabe.[68] The spin-Hamiltonian follows the form of the crystalline field

$$b_2^0 S_z^2 + \frac{7}{12} b_4^0 (S_z^4 - \frac{27}{2} S_z^2 + 25 S_z^2) + \frac{1}{120} b_4^3 \left[S_z (S_+^3 + S_-^3) + (S_+^3 + S_-^3) S_z \right]$$

$$+ \frac{b_6^0}{1260} \left[231 S_z^6 - \frac{315 \times 63}{4} S_z^4 + 735 S_z^4 + \frac{105 \times 3969}{16} S_z^2 \right.$$

$$\left. - \frac{525 \times 63}{4} S_z^2 + 294 S_z^2 \right]$$

$$+ \frac{b_6^3}{5040} \left[(11 S_z^3 - 3 S_z \cdot \frac{63}{4} - 59 S_z)(S_+^3 + S_-^3) \right.$$

$$\left. + (S_+^3 + S_-^3)(11 S_z^3 - \frac{3 \times 63}{4} S_z - 59 S_z) \right]$$

$$+ \frac{b_6}{2520} (S_+^6 + S_-^6)$$

The sixth-order terms are included because the manifold $S = \frac{7}{2}$ can "feel" these terms.

The behavior of the spins under this Hamiltonian is similar to the case of Fe^{3+}. However, the larger spin manifold makes the computation of energies more difficult. The state $m_s = +7/2$, for example, is coupled to the states $+1/2$ and $-5/2$ by the spin-Hamiltonian in zero-field or in an axial-magnetic field H_z. The resulting third-order algebraic equation can be solved rigorously, but the expressions are too unwieldy to be useful. The energy levels in an axial magnetic field by

first-order perturbation are:[18]

$$m_s = \pm\frac{7}{2}: \quad \pm\frac{7}{2}g\beta H + 7b_2^0 + 7b_4^0 + b_6^0$$

$$m_s = \pm\frac{5}{2}: \quad \pm\frac{5}{2}g\beta H + b_2^0 - 13b_4^0 - 5b_6^0$$

$$m_s = \pm\frac{3}{2}: \quad \pm\frac{3}{2}g\beta H - 3b_2^0 - 3b_4^0 + 9b_6^0$$

$$m_s = \pm\frac{1}{2}: \quad \pm\frac{1}{2}g\beta H - 5b_2^0 + 9b_4^0 - 5b_6^0$$

The calculation is immeasurably simplified by referring to the tables given by Stevens.[24]

The value of g is always very close to but slightly less than 2 for all spectra measured to date.[20,21] As in the case of Fe^{3+}, the quadratic term is the largest term in the Hamiltonian. However, the degree of dominance of this term is highly variable from crystal to crystal. Ratio $b_4^0/b^0{}_2$ varies from 1/50 in the ethyl sulfate to 1/8 in the trichloride. Even when this ratio is small, the contribution to the energy from the higher terms is not negligible. This can be seen from the energies of $m_s \pm 5/2$ in an axial field.

The spectrum has a three-fold variation with ϕ. However, it is not a pure sinusoid. The two sites in the unit cell give rise to different spectra which coincide only when the magnetic field lies in a vertical plane containing one of the rhombohedral axes of the unit cell. This is the same as Fe^{3+}. It differs from Fe^{3+} on the equator ($\theta = 90^\circ$). The term which is equivalent to Y_4^3 vanishes, but the term which is equivalent to Y_6^6 has a maximum here. Therefore, a six-fold variation in the spectrum should be

observed here. The two spectra should then coincide every 30 degrees in ϕ and attain their maximum divergence midway between the points of coincidence. However, b_6^6 may be very small, in which case this effect may be too small to be detected. The behavior of the energy levels in an axial magnetic field is shown in Fig. 19.

The hyperfine structure due to the odd isotopes Gd^{155} and Gd^{157} have been observed. The hyperfine splitting is about 5 gauss. The intensity is about 1/20th of the line intensity due to the even isotopes.

2.4 The Experiment and Results

Several samples of calcite from Rodeo and Chihuahua in Mexico and from Imperial County in California were tested for impurity content by both paramagnetic resonance and by spectrographic analysis. The original intent was to select the purest crystal possible. In the course of these tests it was noted that some samples showed small but sharp resonances at very low magnetic fields. The pure crystals which were selected were used for neutron-irradiation by J. Kemp and for diffusion of iron, nickel and chromium by the author. When the efforts towards diffusion failed, the crystals were rechecked for maximum resonance at low field. The resonance intensity of the low field line was fairly constant from sample to sample. In contrast, a large difference in manganese content was observed.

Two large crystals of approximately 15 cc each were selected for the strength of the low field resonance and the

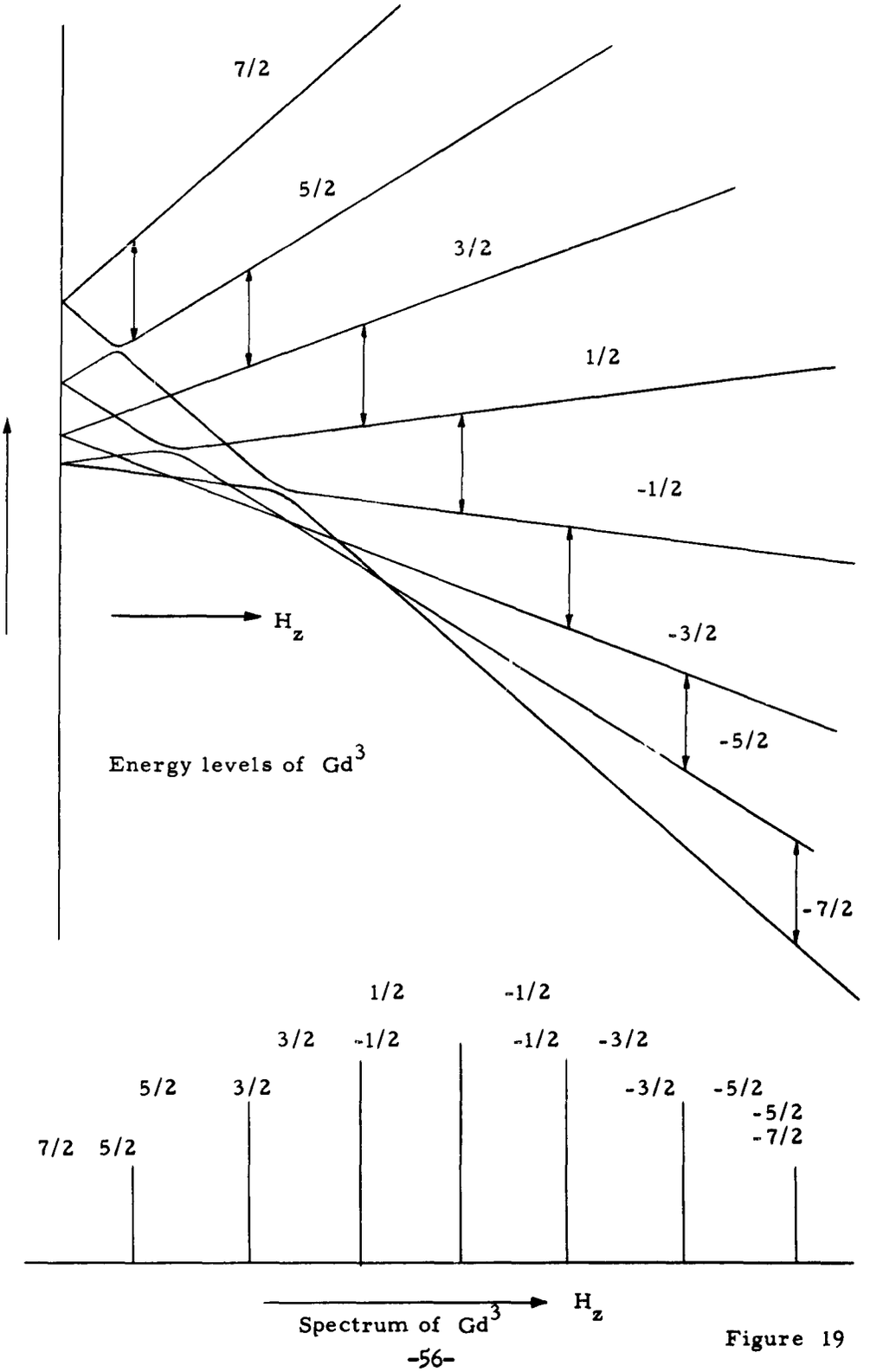
7/2
5/2
3/2
1/2
-1/2
-3/2
-5/2
-7/2
H_z
Energy levels of Gd^3
1/2
-1/2
3/2
-1/2
-1/2
-3/2
5/2
3/2
-3/2
-5/2
-5/2
-7/2
7/2
5/2
H_z
Spectrum of Gd^3

Figure 19

relative absence of manganese.

One crystal was cut into slabs of approximately 3/16" thickness. The slabs were parallel to the plane formed by the C-axis and one of the rhombohedral axes vectors. The orientation was determined by the cleavage planes. It is accurate to perhaps 2 degrees. The C-axis was scratched on the slab. This can also be determined by the cleavage surfaces. The C-axis should be 63.75° from one cleavage surface and 45.5° from the intersection between the other two cleavage surfaces. When the magnetic field is in this plane, the spectra due to the two non-equivalent sites coincide.

The other crystal was also cut into slabs which included the C-axis but rotated 30° about the C-axis. When the magnetic field lies in this plane, the spectra due to the two non-equivalent sites should show the maximum divergence.

In addition, a slab of Rodeo calcite with the C-axis normal to the slab was kindly provided by Dr. J. C. Kemp.

A series of spectrographic analysis carried out on the samples by G. Gordon showed the following impurities.

Source	Mn^{2+} %	Fe %	Mg %	Boron %
Chihuahua, Mex.	$<$.001	.002 max.	.02	0
Rodeo, Mex.	$<$.001	.002 max.	.01	0
Crestmore, Calif. (Blue)	.02	.004	.2	.004

Unfortunately, this method of analysis has very poor sensitivity

for rare earths. Therefore, the absence of detection is not significant. The minimum detectable amount of rare earths is about .05% by weight.

It is significant that most samples show a small amount of iron. $FeCO_3$ (siderite) is a well-known natural mineral with the same crystal structure as calcite and with fairly close lattice dimensions. They are close enough so that an extensive series of mixed crystals $FeCO_3$:$CaCO_3$ is found.[69] This isomorphism between $FeCO_3$ and $CaCO_3$ plus the fact that iron is the most abundant magnetic substance in the earth's crust makes it the most likely paramagnetic impurity besides Mn in calcite.

At room temperature a total of ten principal resonance lines are observed with an axial-magnetic field. In addition, a very large number of resonances appear in the neighborhood of free-spin resonance. These lines are temporarily ignored because they are of no interest in three-level masers. The other lines were observed in detail at 77°K to obtain a better signal-to-noise ratio. The spectrum changes somewhat upon cooling, indicating a temperature dependence of the spin-Hamiltonian parameters. However, there is no change in the essential characteristics of the spectrum. All the results reported hereafter are at 77°K, if not otherwise stated.

The results of measurements at x-band in an axial magnetic field are contained in Figures 20 and 21. The accuracy of magnetic field value is dependent on the accuracy of the magnet current reading. This is about .002 which is about 8 gauss. Line

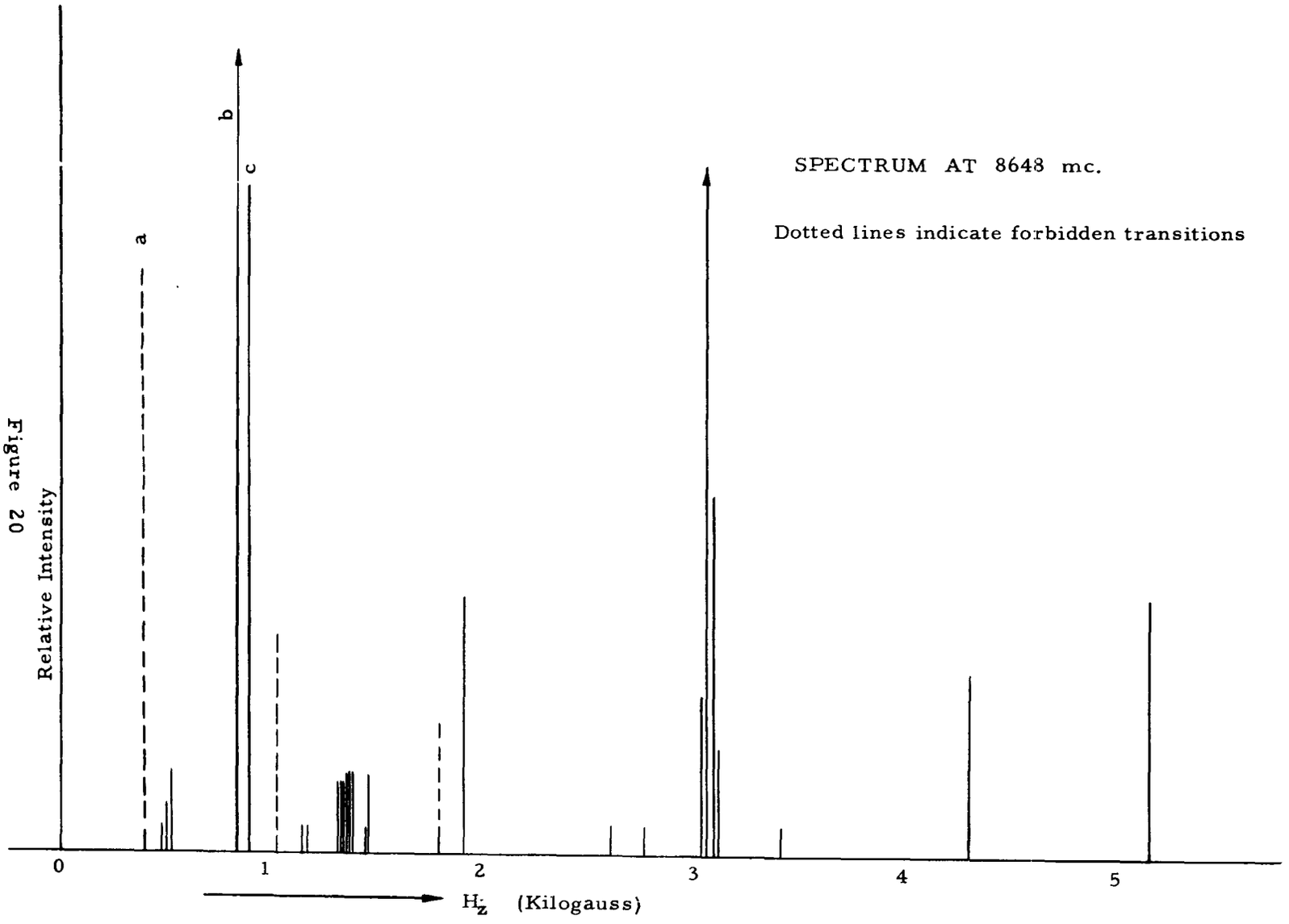
SPECTRUM AT 8648 mc.
Dotted lines indicate forbidden transitions
a
b
c
Relative Intensity
0
1
2
3
4
5
H_z (Kilogauss)

Figure 20

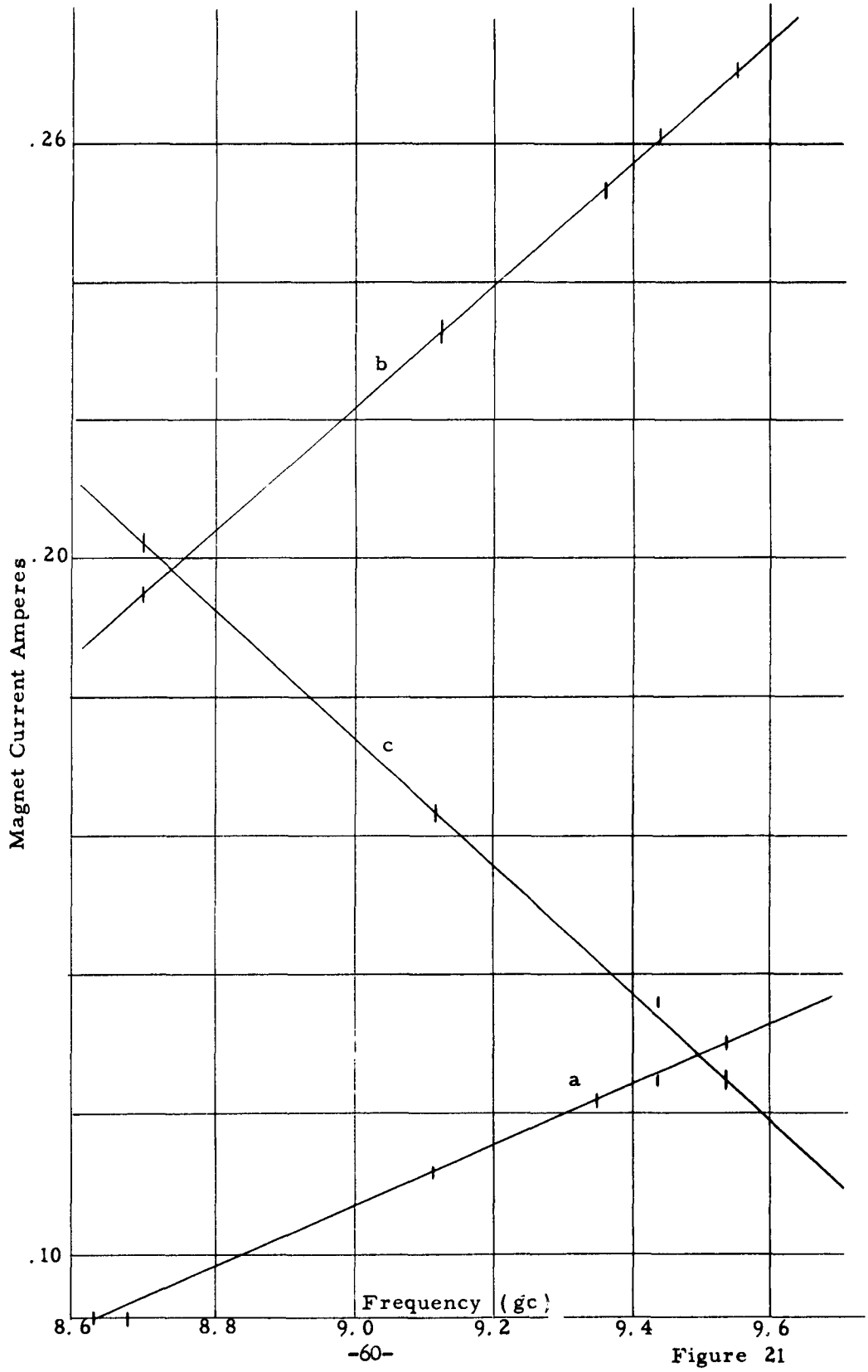
.26
.20
.10
Magnet Current Amperes
b
c
a
8.6
8.8
9.0
9.2
9.4
9.6
Frequency (gc)

Figure 21

widths can be measured to considerably better precision because it is obtained from the width as recorded on the strip chart and converting to magnetic field by the known field and chart sweep rates. This rate is known within 10%. The line widths are, likewise, accurate to within 10%.

When the second-order terms in the energy arising from the cubic term in the spin-Hamiltonian are ignored, the points should fall on a straight line. As the figures show, the measured points do not fall on a straight line. The deviation from the best straight line through the points is larger than the estimated error in the measurements. This is probably due to the inaccuracy in the crystal orientation. This can come about both in the process of cutting the crystal and in the process of mounting the crystal in the cavity.

The slope of the straight line is related to the effective g-factor by the following relation:

$$1.4\, g_{eff.} = \Delta f / \Delta H$$

Lines belonging to the same paramagnetic impurity spectrum should have identical g-factors. The effective g-factors calculated in this manner are 3.84, 1.93 and 1.99 for the lines a, b and c in Figure 21.

Line a has no intensity when the magnetic field is exactly on the C-axis. (Its position is obtained as the limit as the magnetic field approaches the C-axis.) The large effective g-factor provides the explanation. It is a "forbidden" transition

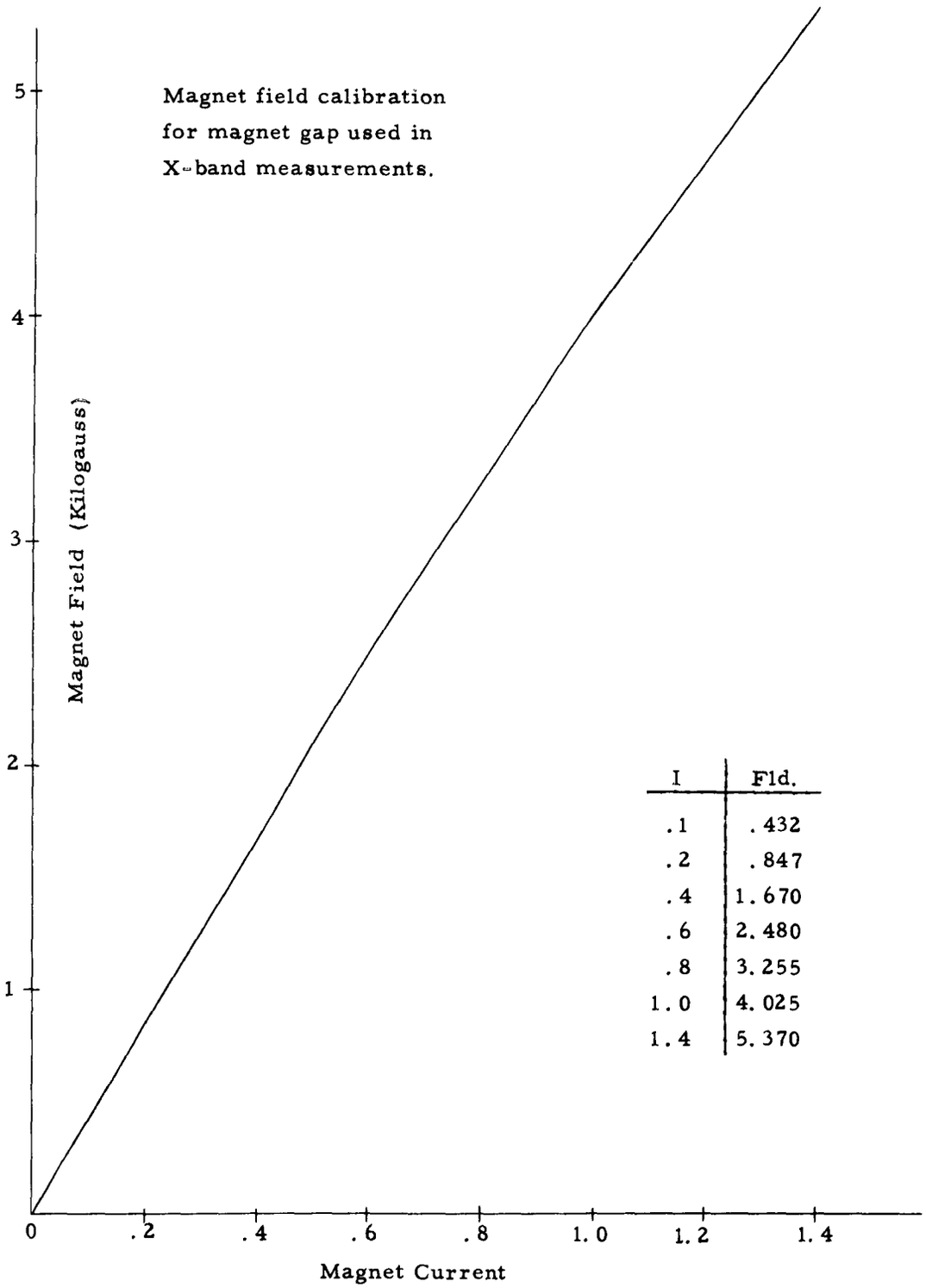

I	Fld.
.1	.432
.2	.847
.4	1.670
.6	2.480
.8	3.255
1.0	4.025
1.4	5.370

Figure 22

with a double quantum jump ($\Delta m = 2$). The true g-factor for the line is one-half of the measured value. Therefore, the corrected effective g-values are 1.92, 1.93 and 1.99.

The best straight line can be extrapolated to zero field to estimate the zero-field splittings. The values obtained for the three lines are 6540 mc, 6570 mc and 11000 mc for a, b and c. The first two values are within experimental error. It seems reasonable to assume that they are the same.

The arrangement of energy levels suggested by these measurements is shown in Figure 23. This type of energy configuration can only result from a half-integral spin S. An integral value of S results in the configuration shown in Figure 24. In such a configuration, we cannot have a $\Delta m = 2$ transition and a $\Delta m = 1$ transition beginning with the same zero-field splitting. From this we conclude that, if the three lowest lines a, b and c, belong to a single spectrum, the spectrum is that of a half-integral S. Furthermore, the fact that two allowed transitions are observed between 0 and 3000 gauss indicates that the value of $S = 5/2$. The lines are also observed to split when the magnetic field is not in the glide plane of the crystal. This indicates a ϕ-variation of the spectrum and leads to the conclusion that the spin is at least 5/2. Actually, many other resonances are observed, but none of sufficient intensity to be included in this spectrum.

The assignment of $S = 5/2$ is made, nevertheless, with great reluctance, for this value of spin is only possible for

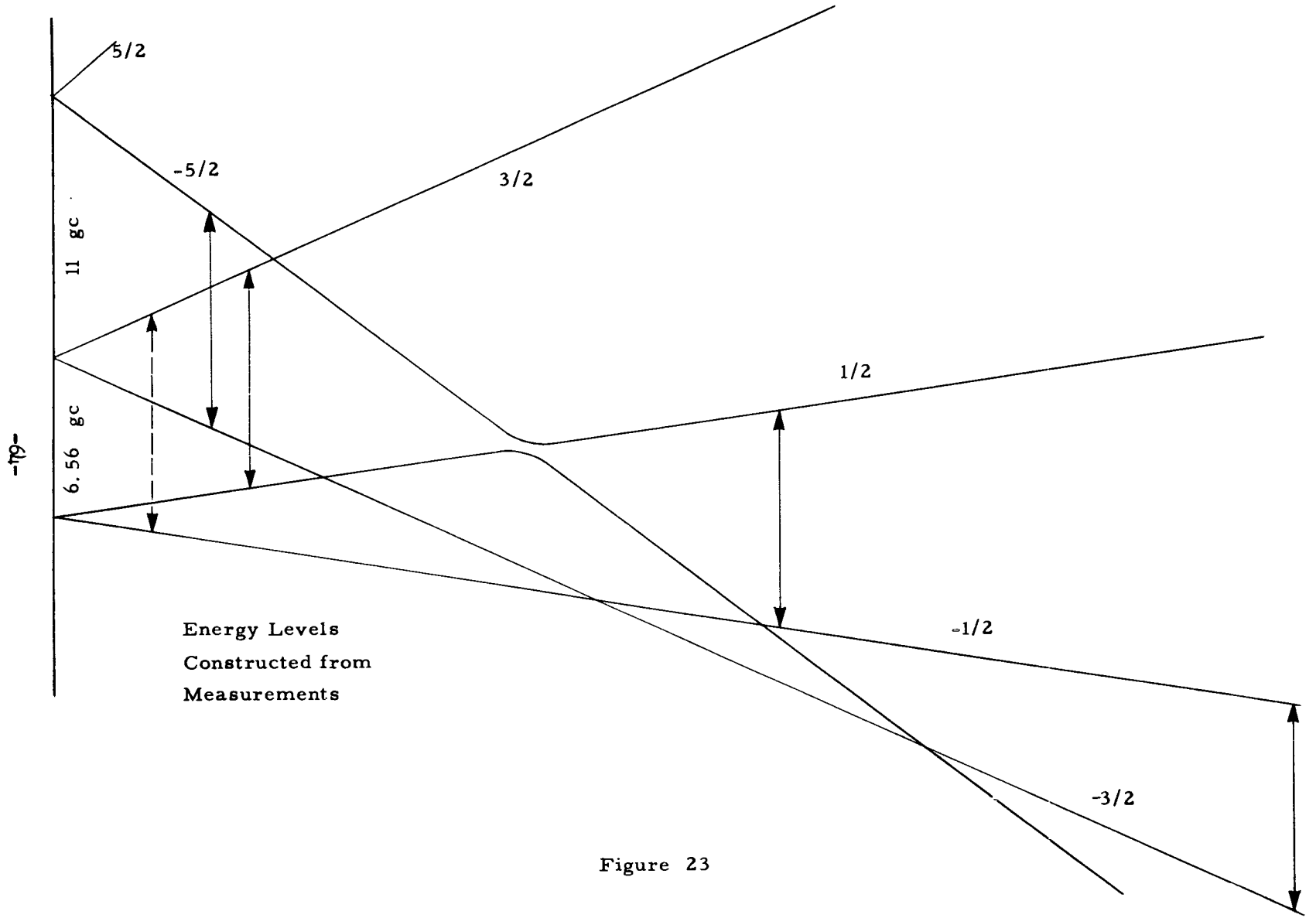
5/2
-5/2
3/2
11 gc
6.56 gc
1/2
-1/2
-3/2
Energy Levels
Constructed from
Measurements

Figure 23

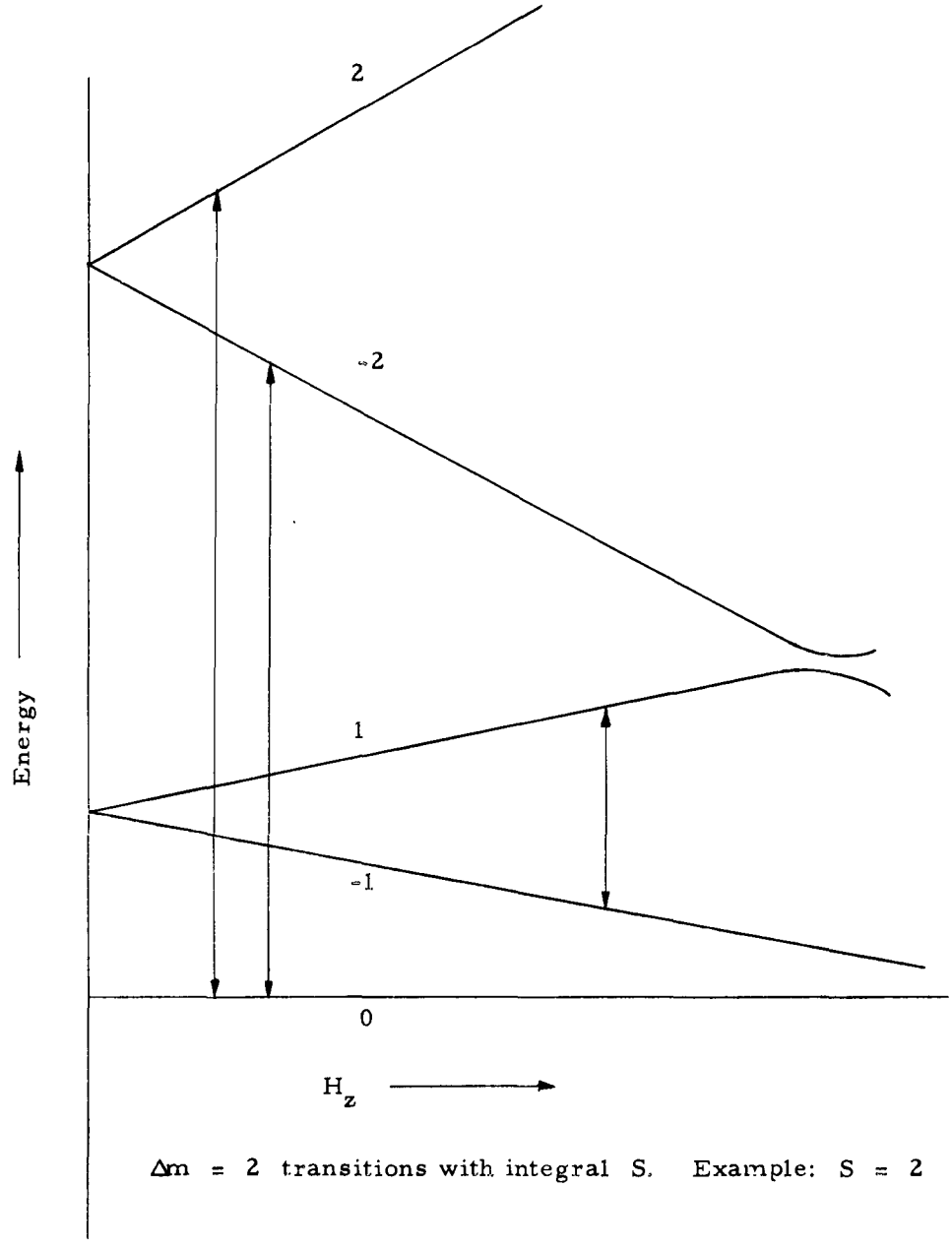

$\Delta m = 2$ transitions with integral S. Example: S = 2

Figure 24

either Fe^{3+} or Mn^{2+}. The spectrum of Mn^{2+} in calcite has already been reported.[71] It is clearly visible in these samples and cannot be confused with the resonances in question. Therefore, Fe^{3+} is indicated as the source of these resonances. But we have already noted that an isomorphic crystal $FeCO_3$ (siderite) exists. It is difficult to believe that an iron impurity in calcite would be trivalent. Another cause for the reluctance is the surprising strength of the "forbidden" lines. When the magnetic field is 20 degrees away from the C-axis, it appears to become comparable or stronger than some "allowed" transitions. When the zero-field splitting is comparable to the Zeeman energy, strong "forbidden" transitions are expected. The calculated transition probabilities in ruby[71] show transition intensities up to about 1/3 of the "forbidden" lines. The strength of the lines observed here seems to be somewhat unreasonable.

Before making a definite identification, three possibilities must be eliminated. They are:

1. The possibility that the lines do not belong to the spectrum of a single impurity.
2. The possibility that the lines belong to the spectrum of a single impurity whose lattice sites are distorted differently by Jahn-Teller effect or by charge compensation.
3. The possibility that the spectrum belongs to some ion outside the iron group.

To check the first possibility, two additional pieces of calcite from Mexico were checked to see if any variation in the

relative strength of the lines could be observed. The same check was performed on a sample of blue calcite provided by Professor Myers of the Department of Chemistry. The source is Crestmore, California, a site completely unrelated to the Mexican sources. The relative intensities in the different samples were in fair agreement. This does not rule out the possibility that the resonances belong to more than one impurity, but it is unlikely.

The second possibility was checked by observing the variation in the resonance when the magnetic field was rotated normal to the C-axis. The positions of the resonances were almost constant. The largest variation was of the order of a line width ($\sim$ 2 to 5 gauss). These variations can be explained by a slight misalignment of the crystal. There was no evidence to indicate anything but a trigonal field whose axis coincided with the C-axis.

The third possibility is difficult to rule out entirely. However, a reasonable case can be made. Any ion which is to account for the observed spectrum must have a relatively long relaxation time and a g-value close to 2. It must have a very small nuclear moment of low abundance if any. It must be either divalent or trivalent and possess a spin equal to or larger than 5/2. A quick check of the list of paramagnetic ions reveals Gd^{3+} as the only probability. It has a spin of 7/2.

To account for the spin of 7/2 in Gd^{3+} one more resonance line must be found below the free-spin value. Such a line does exist at 1.9 kilogauss as shown in Figure 20. However, this line

is accompanied by two fairly prominent hyperfine lines which are absent in the lines discussed up to this point. The intensity is also too small. The possibility remains that the zero-field splitting between the levels $m_s \pm 7/2$ and $m_s \pm 5/2$ in Gd^{3+} is too large for resonance to be observed at 9 gc. This possibility was serious enough to warrant an investigation at a higher frequency. The observed resonances at k-band are given in Fig. 25. The agreement with the x-band measurements is fairly good. No additional resonances were observed. Therefore, Gd^{3+} is ruled out. The k-band measurements are discussed in more detail in the next section.

With all the obvious alternatives explored and rejected, there is little choice but to accept Fe^{3+} as the impurity whose spectrum is observed. This acceptance is made immeasurably easier by the report by M. Peter, et al.[12] on the spectrum of Fe^{3+} in $MgWO_4$, $ZnWO_4$ and $CdWO_4$. This report is interesting because the three tungstate crystals are nearly isomorphic with another tungstate $FeWO_4$. The situation here is analogous to the isomorphism between $CaCO_3$ and $FeCO_3$. Furthermore, a measurement of spin population by comparison to the resonance due to 13 mg of $CuSO_4$ yields a value of 5×10^{15}. This corresponds to a density of about 10^{-4}% which is far below the figure for iron obtained by spectrographic analysis. This would seem to indicate that only a small amount of the total iron content is in the trivalent state.

The spectrum of Fe^{3+} in a trigonal symmetry was given in Section 2.2 and Figure 16. It consists of the largest central

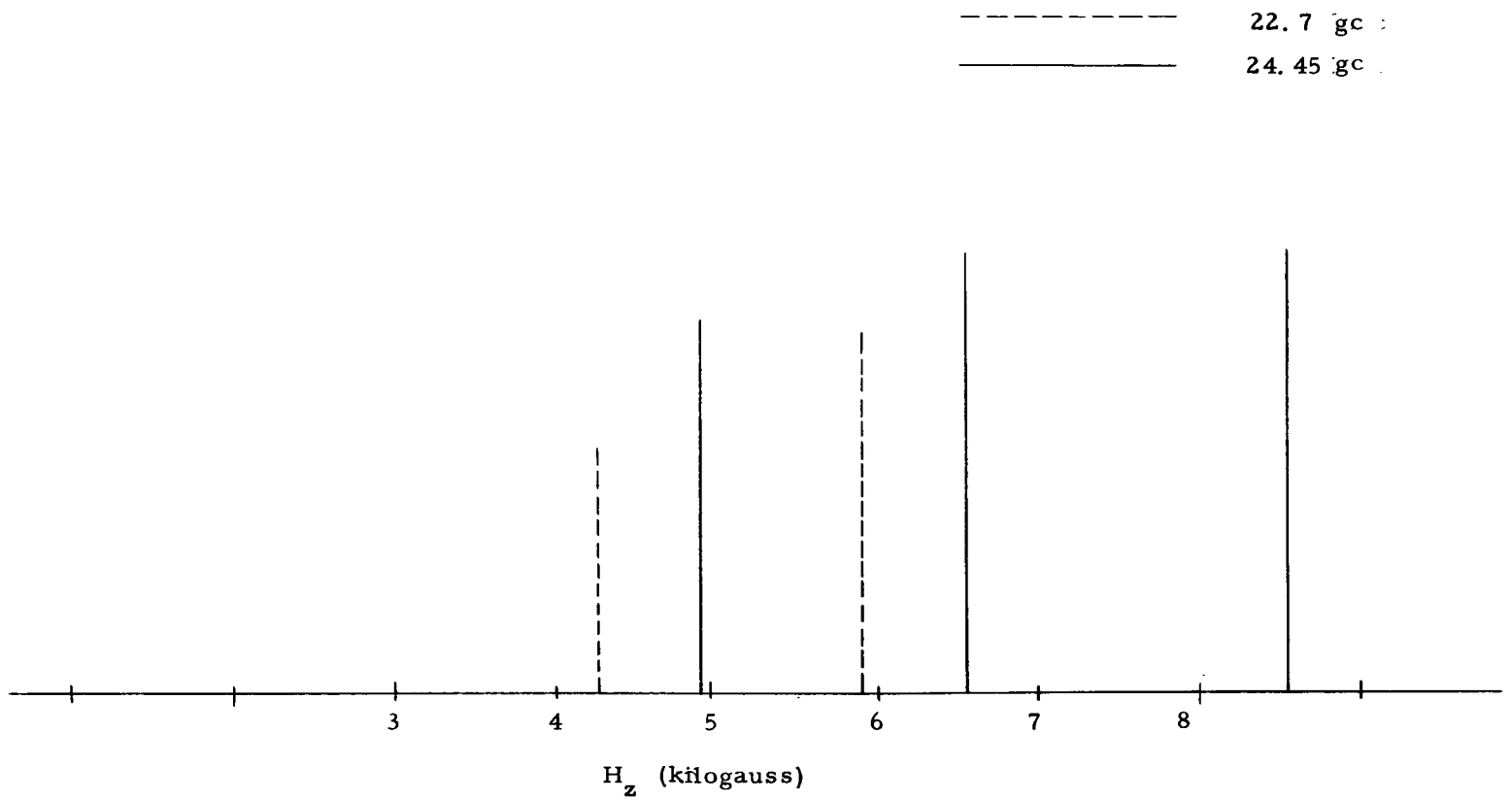

Resonances in Calcite at K-band

Figure 25

line flanked by two lines on either side in roughly symmetric positions. Assuming that the two lowest lines in the figure correspond to the two lowest observed lines, the presence of the other three lines must be established.

In the region where the strong central line is expected, at least three resonances are observed. The strongest of the three is easily saturated and isotropic. This cannot belong to the spectrum of Fe^{3+}. The weaker of the remaining two lines can be identified with another spectrum, probably that of Cr^{3+}. The third line is definitely not isotropic and must be associated with the spectrum of some spin multiplet. The intensity of this remaining line is about 1/3 of the intensity required of the $m_s = +1/2$ to $-1/2$ transition in Fe^{3+}. Yet there is no other spectrum present with which this spectrum can be associated. The g-factor is 2.00 if higher order effects are ignored.

The line which may correspond to the next higher transition $m_s = -1/2 \longleftrightarrow -3/2$ is observed at 5415 g at 8997 mc. The position is very close to the expected value. It has a slope giving a g of approximately +2. Unfortunately, the intensity is approximately 1/5 of the required value.

No measurement of any line corresponding to the $m_s = -3/2 \longleftrightarrow -5/2$ transition at high fields was possible because the required magnetic field exceeds the capacity of the magnet used in the experiment.

To sum up the evidence obtained from measurements obtained at x-band, we can enumerate the following points:

1. The lines at low field indicate that the spectrum belongs to Fe^{3+}.
2. The effective g-factors at low fields are not consistent.
3. High field lines are detected in approximately the expected positions, but the intensities are well below the expected values. The g-factors computed from these lines are substantially higher than values computed from the low field lines.

Measurements at k-band show a qualitative agreement with the results at x-band. The data at k-band were obtained partly from a k-band paramagnetic spectrometer assembled by the author and partly from a spectrometer in the Department of Physics. The spectrometer assembled by the author had superior sensitivity but was limited in usefulness by the very limited magnetic field available (7.5 kilogauss). This does not permit the observation of the $m_s = +1/2 \longleftrightarrow -1/2$ transition. The other spectrometer is equipped to observe very wide resonance lines. It could not be re-arranged conveniently to observe the narrow lines encountered in these measurements. There is also some question about the magnetic field calibration. The accuracy of the measurements is probably poor.

The results of measurements at k-band are given in the following table:

	Magnetic Field		
Frequency	$+5/2 \leftrightarrow +3/2$	$+3/2 \leftrightarrow +1/2$	$+1/2 \leftrightarrow -1/2$
22,700	4260 g	5900 g	-
24,450	4910 g	6565 g	8550 g

The measurement at 22.7 gc was made with the author's spectrometer. The $m_s = +1/2 \leftrightarrow -1/2$ transition could not be observed because the magnetic field was too low. This transition is observed at 24.45 gc at a field which indicates a g-factor of 2.05. On the other hand, estimates of the g-factor by taking the slope $\Delta f / \Delta H$ yields $g = 1.88$ for the line $m_s = 3/2 \leftrightarrow 1/2$ and $g = 1.92$ for $m_s = 5/2 \leftrightarrow 3/2$. The agreement with the results at x-band is only fair. The zero-field splittings using a mean g-value of 1.9 are 7 gc and 11.3 gc. These results are in poor agreement with the x-band results.

The most interesting result of the k-band measurements is the relative intensities of the various lines. At this frequency, the intensities follow more closely the required intensity ratios. The measured intensities at 24.45 gc were in the ratio 9:11:11 for the $+5/2 \leftrightarrow +3.2$, $+3.2 \leftrightarrow +1/2$, $+1/2 \leftrightarrow -1/2$ transitions.

The measurements at k-band are crude and incomplete. The numerical results of these measurements are in fair to poor agreement with the results at x-band. Yet, in spite of these weaknesses, they seem to substantiate the assumption that the observed spectrum is that of Fe^{3+}. In this light, the observed deviation of the ratio of the fine structure line intensities

from the theoretical value requires some explanation.

The deviation of the relative intensities of the fine structure lines from their theoretical values can occur for two reasons according to Bleaney.[73] One source of such deviations is the imperfections in the crystal which produce a variation in the crystalline field strength at the paramagnetic impurity sites. This produces a variation in the zero-field splitting which broadens and reduces the intensities of the lines whose positions involve a large amount of zero-field splitting (lines far from the free spin resonance position). Another source of line intensity deviation is the crystalline imperfections which do not necessarily affect the crystalline field strength, but cause a variation in the direction of the crystalline field. In this case, the effect is proportional to the applied magnetic field. There is no broadening or reduction in intensity at zero-field and a very strong reduction at high fields. Both types of deviations are expected in most natural crystals.

There is ample evidence that both types of crystalline imperfections are present in the samples of calcite examined in this work. Strong evidence of the imperfections of the first type can be seen in the observed spectrum of Mn^{2+} (Fig. 26). Instead of the theoretical ratio of 9:8:5 for the fine structure lines, the observed ratio was usually about 9:3:0. In fact, the effect seems to be so strong here that it is almost unbelievable. It is possible that another, yet unknown, mechanism is responsible for at least some of this deviation. It was found that the

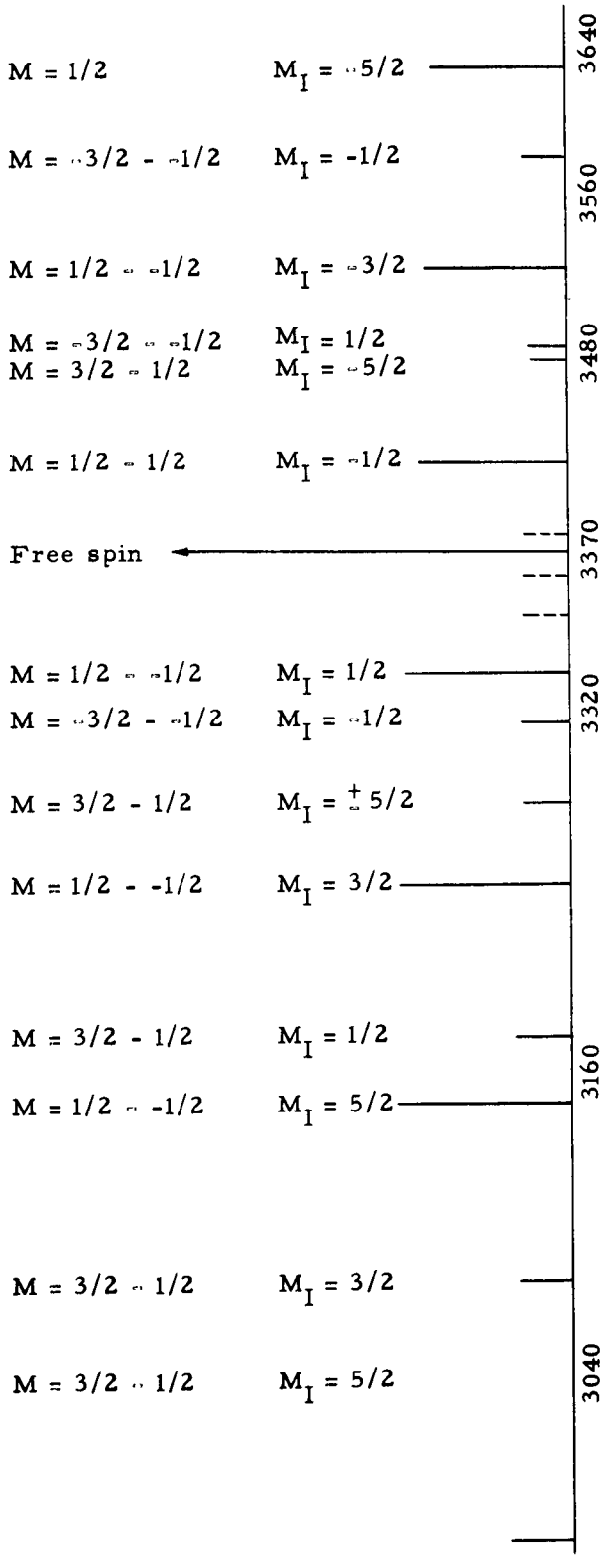

Portion of the Spectrum of Mn^{2+} at 9450 Mc

Figure 26

blue-white calcite samples from Crestmore displayed a manganese spectrum which was closer to the theoretical spectrum. Yet, these samples were very obviously imperfect. They are an opaque blue, streaked with white and show many small cracks and curved cleavage surfaces. In contrast, the calcite samples used for the examination of the Fe^{3+} spectrum are colorless and transparent, completely free from fractures and possess perfect cleavage surfaces. Spectrographic analysis also showed them to be exceptionally pure. One possible explanation is that the lines in the blue calcite, while possessing large line broadening due to imperfections, possesses an even larger homogeneous line broadening due to the high Mn^{2+} concentration. Therefore, the imperfections do not alter the line strengths. In the Rodeo samples, the low Mn^{2+} concentration (not detectable spectrographically) leads to a very small homogeneous broadening. The much larger broadening due to imperfections has a drastic effect on the line strengths. The second type of imperfection is also evident in the manganese spectrum. The hyperfine lines which extend over approximately 500 gauss show a gradual decrease in amplitude as the magnetic field is increased. The total decrease over the hyperfine spectrum varies from 20 to 50%.

The observed intensity relations in the Fe^{3+} spectrum at x-band are:

1. The $m = 1/2 \leftrightarrow -1/2$ transition is about 1/3 of the intensity required by the $m = 3/2 - 1/2$ transition.

2. The $m = -1/2 \leftrightarrow -3/2$ transition is about 1/5 of the intensity required by the $m = 3/2 - 1/2$ transition.
3. The $m = -5/2 \leftrightarrow -3/2$ transition is slightly weaker than the theoretical value of .625 of the intensity of the $m = 3/2 - 1/2$ line.
4. The $m = -5/2 \leftrightarrow -3/2$ and the $m = -3/2 - -1/2$ lines appear to be broadened. This is particularly true for the latter.

The two crystalline defect effects seem to provide a satisfactory explanation for these facts. It would appear that the variation in the field direction is the dominant source of the relative intensity deviations.

One more evidence is present which lends support to the assumption that the spectrum is that of Fe^{3+}. When very high gain is used to record the strongest lines, a small hyperfine line appears on either side of the lines. This can be interpreted to be due to a nuclear spin of 1/2 with an abundance of about 1%. The hyperfine splitting is approximately 10 gauss. This agrees fairly closely with the hyperfine structure of Fe^{57} recently measured by Woodbury.[64] He found $I = 1/2$ and $A \sim 12$ gauss. The abundance is 2.2%. Silver is the only other paramagnetic ion which has a nuclear spin of 1/2. The abundance is 100% and is, therefore, safely ruled out.

2.5 Evaluation of the Spin-Hamiltonian Parameters

If Fe^{3+} is assumed to be the impurity which is the source of the observed spectrum, the spin-Hamiltonian must have the form

$$\mathcal{H}_s = g\beta\bar{H}\cdot\bar{S} + DS_z^2 + \frac{7}{36}(-a+F)(S_z^4 - \frac{95}{14}S_z^2) - \frac{\sqrt{50}a}{180}\left\{S_z(S_+^3 + S_-^3) + (S_+^3 + S_-^3)S_z\right\} \tag{2.7}$$

For a d.c. magnetic field in the z-direction, the eigen-energies and eigen-states can be obtained exactly because the spin-Hamiltonian matrix factors into three 2 x 2 matrices. Namely, the only mixing of eigen-states of S_z is due to the three-fold term. This term mixes states which differ by $\Delta M_s = 3$. Thus, states $M_s = +5/2$ and $-1/2$ mix exclusively with each other. States $M_s = -5/2$ and $+1/2$ mix exclusively with each other. States $M_s = +3/2$ and $M_s = -3/2$ remain pure because $(3/2|\mathcal{H}_s|-3/2) = 0$ for this particular Hamiltonian and $S = 5/2$. The eigen-energies are given by

$$E_{1,2} = \frac{E^o_{5/2} + E^o_{1/2} + 2g\beta H \pm \sqrt{(E^o_{5/2} - E^o_{1/2} + 3g\beta H)^2 + \frac{20}{9}a^2}}{2}$$

and

$$E_{3,4} = \frac{E^o_{5/2} + E^o_{1/2} - 2g\beta H \pm \sqrt{(E^o_{5/2} - E^o_{1/2} - 3g\beta H)^2 + \frac{20a^2}{9}}}{2} \tag{2.8}$$

Here

$$E^o_m = Dm^2 + \frac{7}{36}(-a+F)\left[m^4 - \frac{95}{14}m^2\right]$$

which is the zero-field energies in the absence of the three-fold terms.

Each of the new energy levels can be considered to be a perturbation on the levels in the absence of the three-fold term. The correspondence is

Perturbed Energy	Zero-field Energy with 3-fold term
E_1	$E_{5/2}$
E_2	$E_{-1/2}$
E_3	$E_{-5/2}$
E_4	$E_{+1/2}$

If $\underline{a}$ is small compared to $E_{5/2} - E_{1/2} \pm 3g\beta H$, the energies can be approximated by

$$E_1 \cong E_{5/2} + \frac{5}{2} g\beta H + \frac{5a^2}{9(E_{5/2} - E_{1/2} + 3g\beta H)}$$

$$E_2 \cong E_{1/2} - \frac{1}{2} g\beta H - \frac{5a^2}{9(E_{5/2} - E_{1/2} + 3g\beta H)}$$

$$E_3 \cong E_{5/2} - \frac{5}{2} g\beta H + \frac{5a^2}{9(E_{5/2} - E_{1/2} - 3g\beta H)}$$

$$E_4 \cong E_{1/2} + \frac{1}{2} g\beta H - \frac{5a^2}{9(E_{5/2} - E_{1/2} - 3g\beta H)}$$

$$E_5 = E_{3/2}$$

$$E_6 = E_{-3/2} \qquad (2.9)$$

The energy differences for allowed transitions are as follows:

1)

$$E_{\frac{1}{2}} - E_{-\frac{1}{2}} \simeq E_4 - E_2 = g\beta H - \frac{5a^2}{9}\left(\frac{1}{E_{5/2} - E_{1/2} - 3g\beta H} - \frac{1}{E_{5/2} - E_{1/2} + 3g\beta H}\right)$$

$$= g\beta H - \frac{5a^2}{3}\left(\frac{2g\beta H}{(E_{5/2} - E_{1/2})^2 + 9g^2\beta^2 H^2}\right)$$

$$= g\beta H - \frac{10a^2 g\beta H}{3\left[(E_{5/2} - E_{1/2})^2 + 9g^2\beta^2 H^2\right]} \qquad (2.10)$$

This shows that this resonance occurs at a frequency which is lower than that given by $g\beta H$ alone.

2)

$$E_3 - E_{3/2} = E_{5/2} - E_{3/2} - g\beta H + \frac{5a^2}{9(E_{5/2} - E_{1/2} - 3g\beta H)} \qquad (2.11)$$

In the low field range where $E_{5/2} - E_{1/2} \gg 3g\beta H$, we can approximate this energy differency by

3)

$$E_3 - E_{3/2} \simeq E_{5/2} - E_{3/2} - g\beta H + \frac{5a^2}{9(E_{5/2} - E_{1/2})} \cdot 1 + \frac{3g\beta H}{2(E_{5/2} - E_{1/2})} \qquad (2.12)$$

Thus, for low fields the effective g-factor

$$g_{eff} = \frac{\partial(\Delta E)}{\partial(\beta H)} = -g + \frac{5a^2}{18(E_{5/2} - E_{1/2})} \cdot 3g$$

$$= g\left(-1 + \frac{5a^2}{6(E_{5/2} - E_{1/2})^2}\right) \qquad (2.13$$

The effective g-factor is a constant and its magnitude is smaller by the factor

$$\frac{5a^2}{6(E_{5/2} - E_{1/2})^2}$$

Finally,

4)

$$E_{3/2^-} E_4 = E_{3/2^-} E_{1/2^+} g\beta H + \frac{5a^2}{9(E_{5/2^-} E_{1/2^-} 3g\beta H)} \tag{2.14}$$

Again, for $E_{5/2^-} E_{1/2} \rangle\rangle 3g\beta H$

$$\Delta E \simeq E_{3/2^-} E_{1/2^+} g\beta H + \frac{5a^2}{9(E_{5/2^-} E_{1/2})} \cdot \left(1 + \frac{3/2g\beta H}{(E_{5/2^-} E_{1/2})}\right) \tag{2.15}$$

The effective g-factor is

$$\frac{\partial(\Delta E)}{\partial(\beta H)} = + g + \frac{5a^2}{9(E_{5/2^-} E_{1/2})^2} \cdot \frac{3}{2} g$$

$$= g \left[1 + \frac{5}{6} \frac{a^2}{(E_{5/2^-} E_{1/2})^2}\right] \tag{2.16}$$

The effective g-factor is a constant and larger than the true g-factor.

5) The "forbidden" transition has the following energy difference.

$$E_{3/2} - E_2 = E_{3/2} - E_{1/2} + 2g\beta H + \frac{5a^2}{9\left[E_{5/2} - E_{1/2} + 3g\beta H\right]}$$

$$= E_{3/2} - E_{1/2} + 2g\beta H + \frac{5a^2}{9} \cdot \left[1 - \frac{3/2g\beta H}{(E_{5/2} - E_{1/2})^2}\right] \tag{2.16}$$

The effective g-value is

$$\frac{\partial(\Delta E)}{\partial(\beta H)} = 2g + \frac{5a^2}{9}\left[-\frac{3/2g}{(E_{5/2} - E_{1/2})^2}\right]$$

$$= 2g - \frac{5a^2 g}{6(E_{5/2} - E_{1/2})^2}$$

$$= g\left(2 - \frac{5a^2}{6(E_{5/2} - E_{1/2})^2}\right) \tag{2.17}$$

For the approximation to be valid, we should have $E_{5/2} - E_{1/2} > 5 \times 3g\beta H$. The approximate value of $E_{5/2} - E_{1/2}$ is 17.5 gc. This requires that H be less than 400 gauss.

These expressions when compared with experimental data should be sufficient to determine the parameters of the spin-Hamiltonian.

Unfortunately, due to the restricted range of frequencies available from the spectrometer, the measurements could not be carried out at sufficiently low fields. The magnetic field values over which most of the measurements were taken were 400 - 1100 gauss. This makes the approximations rather poor. In addition, the accuracy of the measurements themselves is not sufficiently high for a precise determination.

First of all, the g-value is taken to be 2.00, not from the data but from the g-value of Fe^{3+} in all previously known cases. This figure can be considered sufficiently accurate for our purpose.

Next, the zero-field splitting is obtained by extrapolating the lines of Fig. 21 to zero field. The values obtained are

$$E_{-5/2} - E_{-3/2} = 11.03 \pm .18 \text{ gc}$$

$$E_{3/2} - E_{1/2} = 6.55 \pm .2 \text{ gc}$$

The measured value of H_{DC} for the $M_s = +1/2 \longleftrightarrow -1/2$ transition at f = 8997 mc is approximately 3195 gauss. The exact value is not known because there are many strong lines in this region. It is difficult to determine which one corresponds to the Fe^{3+} line. In principle, the value of the constant a can be found from this data because the theoretical energy difference for this transition is independent of D and F as seen from Equation 2.10. ($E_{5/2}$ and $E_{1/2}$ are really dependent on D and F, but they are estimated from measurements.) In practice, the imprecise data makes it almost impossible because we are dealing with a very small difference

$$\frac{10a^2 g \beta H}{3\left[(E_{5/2} - E_{1/2})^2 + 9g^2\beta^2H^2\right]}$$

between the two large quantities; $g\beta H$ and $\Delta E = hf$.

The constant a can also be evaluated by comparing the effective g-values of Equations 2.16 and 2.13 to the slope of

lines b and c in Fig. 21. The effective g-value should be equal to the slope of the lines. It is also independent of D and F if we use the estimated values of the zero-field energies, $E_{5/2}$ and $E_{1/2}$. We note that a reasonably good estimate of a can be made with only approximate values of $E_{5/2}$ and $E_{1/2}$. Again, the source of error is the measurement itself. A comparison of the value of a^2 obtained by the method is given in the table below.

Transition	E	H	g_{eff}	a^2
$-\frac{5}{2} \longleftrightarrow -\frac{3}{2}$	9550 ± 10 − 8700 ±10 = 850 ± 20	304 ± 20g	2.18 − 1.83 C.V. = 1.99	+25 ⟷ −30 C.V. = 1.3
$+\frac{3}{2} \longleftrightarrow +\frac{1}{2}$	850 ± 20	315 ± 20g	g_{eff} = 2.10 − 1.77 C.V. = 1.93	+16 ⟷ (−35) C.V. = −11
$-\frac{1}{2} \longleftrightarrow +\frac{3}{2}$	Δ = 850 ± 20 900 ± 20	168 ± 20g	2.23 − 1.68 C.V. = 1.92	120 ⟷ (−48) C.V. = 45

.14

It is obvious that the data are too crude for a determination of a.

Part of the large discrepancy in the effective g values might be explained by a slight misalignment of the crystal. To investigate this point, perturbation calculations were carried out for energies when the d.c. magnetic field is applied at a small angle θ from the c-axis. The approximate perturbed energies are given by

$$\Delta E_{-5/2 \leftrightarrow -3/2} = E_{5/2} - E_{3/2} - g\beta H\left(1 - \frac{\theta^2}{2}\right) + \frac{5a^2}{9(E_{5/2} - E_{1/2} - 3g\beta H)} + \frac{g^2\beta^2 H^2\theta^2}{4}\left(\frac{10}{E_{5/2} - E_{3/2} - g\beta H} - \frac{8}{E_{3/2} - E_{1/2} - g\beta H}\right) \tag{2.18}$$

$$\Delta E_{+3/2 \leftrightarrow +1/2} = E_{3/2} - E_{1/2} + g\beta H\left(1 - \frac{\theta^2}{2}\right) + \frac{5a^2}{9(E_{5/2} - E_{1/2} - 3g\beta H)} + \frac{g^2\beta^2 H^2\theta^2}{4}\left[\frac{5}{E_{3/2} - E_{5/2} - g\beta H} + \frac{16}{E_{3/2} - E_{1/2} + g\beta H} - \frac{9}{g\beta H}\right] \tag{2.19}$$

$$\Delta E_{+3/2 \leftrightarrow -1/2} = \frac{g^2\beta^2 H^2\theta^2}{4}\left[\frac{5}{E_{3/2} - E_{5/2} - g\beta H} + \frac{8}{E_{3/2} - E_{1/2} + g\beta H} + \frac{8}{E_{3/2} - E_{1/2} - g\beta H} + \frac{9}{g\beta H}\right] + E_{3/2} - E_{1/2} + 2g\beta H + \frac{5a^2}{9\left[E_{5/2} - E_{1/2} + 3g\beta H\right]} \tag{2.20}$$

The error in orientation is considered to be less than 5° at the very most. It is probably less than 2°. However, the perturbation is computed for $\theta = 5^\circ$ ($\theta = 5/57 = .088$ radians).

$$\Delta E_{-5/2 \leftrightarrow -3/2} \cong E_{5/2}-E_{3/2}- g\beta H\,(.9961) + \frac{5a^2}{9\left[E_{5/2}-E_{1/2}-3g(\beta H\right]} + g^2\beta^2H^2(.0078) \left[\ .2\ \right]$$

$$\frac{\partial(\Delta E)}{\partial(g\beta H)} \simeq -.9961g + \frac{5}{6}\frac{a^2}{(17.5)^2}g + .0035g^2\beta H$$

$$= g\ -.9961 + \frac{a^2}{320} + .01H \qquad (2.21)$$

where H is in kilogauss.

At H = 1 kilogauss $g_{eff} = g\left(-.986 + \frac{a^2}{320}\right)$

The effect of even 5° misalignment of the crystal axis reduces g_{eff} by only .028. It is too small to account for the large discrepancy in the measured value of effective g.

For

$$M = +\frac{3}{2} \longleftrightarrow +\frac{1}{2}$$

$$\frac{\partial(\Delta E)}{\partial(\beta H)} = g_{eff} = .996g + \frac{a^2}{320}g\ -.013gH \qquad (2.22)$$

Again, the effect of misalignment is small.

For

$$M = +\frac{3}{2} \longleftrightarrow -\frac{1}{2}$$

$$\frac{\partial(\Delta E)}{\partial(\beta H)} \simeq g_{eff} = 2g(.996) - \frac{a^2}{320}g + gH\cdot(.04) \qquad (2.23)$$

In this case the contribution is not negligible even though it is still small. The effective g-value is larger than the case when the axis is correctly aligned.

It must be concluded that the inconsistency of the measured g-value is due to the poor accuracy of the measurements. It is not possible to obtain any reliable value of the so-called cubic field constant $\underline{a}$ on the basis of these measurements.

There is one way in which the constant $\underline{a}$ can be found even with fairly crude measurements. This is by measurement of the difference in the resonant frequencies for the two non-equivalent sites in calcite.

The two non-equivalent sites are distinguished by the reflection of the spectrum across a plane containing the c-axis. This is equivalent to a relative rotation of the two spectra. The spectrum due to each site has an angular dependence determined by the trigonal part of the spin-Hamiltonian whose amplitude is $\underline{a}$. This part of the Hamiltonian is equivalent to the spatial function $Y_{43} = \sin^3\theta \cos\theta \cos(3\phi + \phi_o)$. If one site is acted upon with a Hamiltonian of the form given above, the other is acted on by a Hamiltonian of the form

$$Y_{43} = \sin^3\theta \cos\theta \cdot\cos(3\phi - \phi_o)$$

These terms have no effect on the spectrum at $\theta = 0$ or at $\theta = 90^o$ because their amplitude is zero. They have the maximum effect around $\theta = \cos^{-1} 1/\sqrt{3}$. If the spectra due to the two sites were measured as a function of the circumferential angle ϕ with $\theta = \cos^{-1} 1/\sqrt{3}$, the two spectra will coincide every 60^o, with a maximum divergence half-way between the points of coincidence. This divergence can be measured directly. Since it

is directly proportional to $\underline{a}$. $\underline{a}$ can be found with good accuracy.

The procedure outlined above requires a magnet with a tilting base so that the d.c. magnetic field can be moved along a cone of angle $\theta = \cos^{-1} 1/\sqrt{3}$. It also requires a sufficiently large magnet gap to accomodate the microwave spectrometer cavity at an angle. It was not possible to carry out such measurements here.

A very approximate determination of the spin-Hamiltonian parameters D and (a-F) is attempted in the basis of the measurements which were possible. This is done by simply extrapolating the lines of Fig. 22 to zero magnetic field. The values of zero-field splittings are

$$E(5/2) - E(3/2) = 11030 \pm 180 \text{ mc}$$

$$E(3/2) - E(1/2) = 6540 \pm 200 \text{ mc}$$

$$E(3/2) - E(-1/2) = 6560 \pm 400 \text{ mc}$$

We can obtain values for D and (a-F) by observing that

$$E(5/2) - E(3/2) \Big|_{H=0} = 4D - \frac{4}{3}(a-F)$$

and

$$E(3/2) - E(1/2) \Big|_{H=0} = 2D + \frac{5}{3}(a-F)$$

The values are

$$a - F = .443 \pm .2 \text{gc}$$

$$D = 2.90 \text{ gc} \pm .06 \text{ gc}$$

The sign of D (and therefore the sign of a-F) is usually determined by examination of relative line strengths at very low temperatures. This was not done in this case because the line strengths here were determined by factors besides the Boltzmann distribution.

The fact that the zero-field splitting and the Zeeman energy are comparable makes reliable perturbation impossible when the magnetic field is not along the c-axis. Furthermore, the trigonal field term $\underset{\sim}{a}$ has an appreciable effect as the field is swung off the crystal axis. However, the behavior of the line positions at $\theta \sim 90^{\circ}$ was found to be in qualitative agreement with the behavior of the line positions predicted by the values of the spin-Hamiltonian given above.

In particular, the appearance of two strong low-field lines ($H \sim .5$ kilogauss) at $\theta \sim 90^{\circ}$ seems to substantiate the interpretation that two doublets $M = \pm 1/2$ and $M = \pm 3/2$ are separated by 6.55 kmc. The two lines result from the fact that the $M = \pm 1/2$ states split into two states given by

$$\psi = \frac{1}{\sqrt{2}}\left(\left| +\tfrac{1}{2} \right\rangle \pm \left| -\tfrac{1}{2} \right\rangle \right)$$

Similarly, the states $M = \pm 3/2$ split into states

$$\psi' = \frac{1}{\sqrt{2}}\left(\left| +\tfrac{3}{2} \right\rangle \pm \left| -\tfrac{3}{2} \right\rangle \right)$$

The latter two states are split by only a very small energy

because there is no direct matrix element connecting $|+3/2\rangle$ to $|-3/2\rangle$. Transitions from $1/\sqrt{2}\,(|+1/2\rangle - |-1/2\rangle)$ are allowed to both $1/\sqrt{2}\,(|+3/2\rangle \pm |-3/2\rangle)$, under microwave excitation, thus giving rise to two closely spaced lines. As θ moves away from 90°, the spacing increases and the intensities become unequal. The effective g-value of these lines at $\theta = 90^{\circ}$ should be approximately 3g.

In addition to the spectrum of Fe^{3+}, one other set of three lines was prominent. This may be due to Cr^{3+}. It was distinguished from the spectrum of Fe^{3+} by a smaller intensity (approximately 1/4) and by the presence of stronger hyperfine lines. The line width is larger. Only one hyperfine line is distinguished clearly on each side. However, the line width is wide enough to conceal an additional pair. In fact, some distortion of the line shape seems to be observable. The over-all hyperfine splitting is about 20 g. This corresponds to $A \sim 7$ gauss, which is smaller than the hyperfine splitting of Cr^{3+} in other crystals. The intensity of the hyperfine line is about 1/35 of the central line. The theoretical value for Cr^{3+} is 1/40.

Assuming that the spectrum belongs to Cr^{3+} (spin is 3/2), the spin-Hamiltonian is simply

$$\mathcal{H}_s = DS_z^2 + g\beta \bar{H}\cdot\bar{S}$$

Here, the higher order terms arising from Koster's treatment are neglected. In an axial magnetic field, the spin states are pure. The g-value can be obtained without approximation.

$$E\beta \left[H_1 + H_2 \right] = 2 \times f$$

H_1 and H_2 are the resonant magnetic fields for the $m_s = +3/2 \longleftrightarrow + 1/2$ and $m_s = -3/2 \longleftrightarrow -1/2$ transitions, respectively. f is the resonant frequency. Using the values at 9450 mc,

$$g = \frac{9450 \times 2}{1.4 \times (4575 + 2195)} = 1.99$$

Alternatively, from the position of the $m_s = +1/2 \longleftrightarrow 1/2$ transition,

$$g = \frac{9450}{1.4 \times 3380} = 2.0$$

The zero-field splitting is just 4575 - 3385 = 1190 gauss.

TABLE OF RESULTS

Ion	g	|D| (gc)	|a-F| (gc)	Zero-field Energies (kmc)
Fe^{3+}	2.00	2.9 ± .06	.45 ± .2	0 6.55 11.03
Cr^{3+}	2.0 - 1.99	1.67	0	0 3.33

2.6 Measurement of T_1

A measurement of T_1 was made by the steady-state saturation method at 77°K. The results were somewhat ambiguous. If the saturation as a function of applied microwave magnetic field follows the solution to Bloch's equation, the saturation should be practically complete with a 10 db increase in

applied power after the inception of saturation. Experimentally, it was found that saturation was much more gradual.

The very gradual saturation is explained in terms of the magnetic field distribution in the TE_{112} circular cavity mode. In this mode there is a spatial variation in magnetic field both in intensity and orientation. The effective microwave magnetic field is just the component normal to the d.c. magnetic field. Thus, there is a very large variation of effective microwave magnetic field intensity over a sample which covers the entire bottom of the cavity. This means that the sample begins saturation where the field is strongest and spreads gradually as the microwave power is increased.

In this situation, we cannot take the saturation power as the point where x" is 1/2 of its maximum value. (For a linear detector, this means that the detected signal is $1/\sqrt{2}$ of the maximum value.) It must be much closer to the value at which the first signs of saturation are observed. This is in the neighborhood of 3 mw. Assuming a cavity Q of 5000 and a line width of 2 gauss, the value of T_1 is approximately 50 μs.

This is fairly short relaxation time but certainly reasonable. Comparison to the reported relaxation times of Fe^{3+} and Cr^{3+} in Al_2O_3 is interesting. The values given are 7 m_s at 4.2°K for Fe^{3+} [63] and 700 μ s at 77°K for Cr^{3+} in Al_2O_3 [51]. Both measurements were made by the pulse-recovery method. The value of 7 m_s at 4.2°K is probably comparable to the relaxation

time of Fe^{3+} in $CaCO_3$ at the same temperature. Cr^{3+} apparently has a much longer relaxation time.

The relaxation time of Fe^{3+} in calcite can also be compared to that of Mn^{2+} in calcite. The spectrum of Mn^{2+} is completely saturated at microwave power levels used to observe the spectrum of Fe^{3+}. A 20 db reduction in power is necessary to produce the Mn^{2+} spectrum. This indicates a relaxation time at least 10 times as long and probably much more. Measurements could not be made at lower power levels because the gain of a detection crystal is severely reduced as the power level drops.

An attempt to measure T_1 by stimulated spin-echoes was not successful. Insufficient sensitivity is believed to be the reason.

CHAPTER 3

BARITE

3.1 Crystal Structure

The following structural information is compiled by Wyckoff[48]. The Crystal structure is orthorhombic with the space group Pnma. The lattice dimensions are a = 8.8625 A, b = 5.442 A and c = 7.140 A. There are four molecules in a unit cell. The atomic positions are

Ba^{2+}, S^{6+} (c) $\pm$ (u, 1/4, v, u+1/2, 1/4, 1/2-v)

O^{2-} (d) $\pm$ (xyz; $\bar{x}$, y+1/2, $\bar{z}$; x+1/2, 1/2 y, 1/2 - z, 1/2 - x, $\bar{y}$, z + 1/2)

For Ba^{2+}

u = .182 v = .161

For S

u = .068 v = .695

The positions of the oxygen ions is not accurately known. James and Wood[75] suggest that the SO_4^{2-} group forms a tetrahedron with S-O spacing of 1.5 A. This gives a O-O spacing of 2.45 A instead of the usual 2.7 A. This is explained by the large attractive force between S and O. The tetrahedrons have one symmetry plane normal to the b-plane and make an angle of 100° with respect to the c-plane. The positions of the atoms are shown in Figure 27.

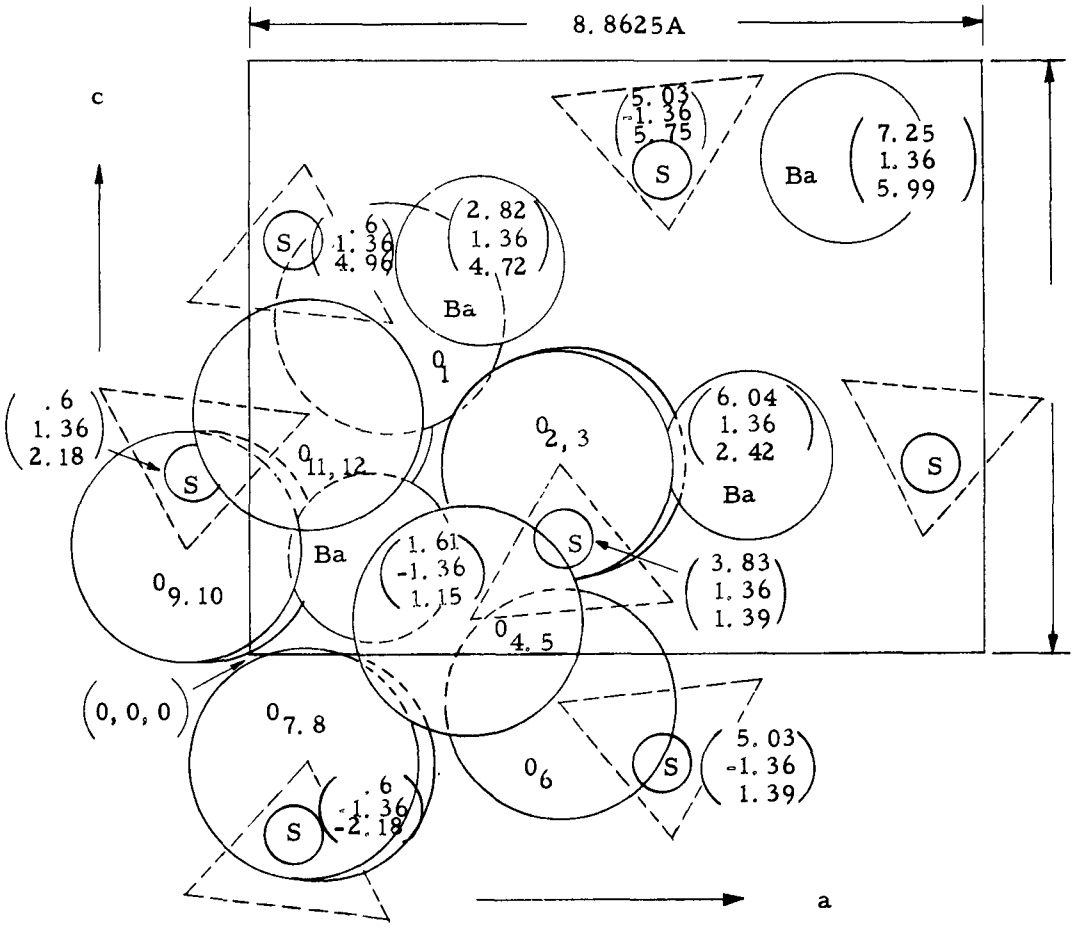

Diagram of a unit cell of BaSO showing the twelve oxygens around one of the barium ions.

Figure 27

The point symmetry of the Ba^{2+} (and S^{6+}) sites is just m. Its reflection plane is normal to the b-axis. The four sites are not unrelated. They are divided into two pairs related by inversion. This follows from the presence of a center of inversion at the center of the unit cell. Two sites which are not related by inversion are related by a vertical glide plane normal to the a-axis. Another glide plane normal to the c-axis follows automatically.

Paramagnetic impurities are expected to substitute Ba^{2+}. The spectra arising from two sites related by inversion are identical. Therefore, the four possible substitutional sites can give two spectra. The two spectra coincide whenever the magnetic field lies parallel to one of the glide planes.

The crystal cleaves very cleanly in the $\{010\}$ and $\{101\}$. The b-axis is located immediately by the $\{010\}$ cleavage. The a-axis is the bisector of the acute angle formed by the $\{101\}$ cleavage surfaces. The c-axis is normal to a and b.

3.2 The Crystalline Field

The radius of Ba^{2+} is given as 1.43 (Goldschmidt), 1.40 (Wasastjerna) and 1.35 (Pauling). In any case, it is a very large ion compared to iron group ions. It is slightly larger than the radius of O^{2-} which is given as 1.35 A. The large radius of Ba^{2+} results in a 12-fold coordination of oxygen atoms around it. The arrangement is highly irregular because the rigid SO_4^{2-} groups restrict the freedom of the oxygens to pack themselves in a regular way about Ba^{2+}. The distances of the oxygens from the Ba^{2+} site

are: two each at 2.78 A, 2.79 A, 2.9 A, 3.08 A and 3.3 A and one each at 2.75 A and 2.87 A.

A calculation of the crystalline field was made by taking just the twelve nearest oxygens as point charges of magnitude -2 e. The result was

$$V = -.0062r^2P_2^0(\cos\theta) + .00724r^2P_2^2(\cos\theta)\cos 2(\phi - 50.6^\circ) - .0004r^4P_4^0(\cos\theta) + .000612r^4P_4^2(\cos\theta)\cos 2(\phi + \theta) + 3.1 \times 10^{-5}r^4P_4^4(\cos\theta)\cos 4(\phi + 12.1^\circ)$$

The fourth order terms are small because of the factor $1/R_i^5$. Nevertheless, their contribution to the total potential is considerable when the factor r^4 is included.

In making this calculation, it is noticed, as in the previous case of calcite, that a large mutual cancellation takes place between the contributions from different oxygens. This effect is illustrated by comparing the net amplitude of a particular term in the expansion to the largest contribution from a single oxygen.

Term in Expansion	Largest Single Contribution	Net Field	Ratio
P_2^0	+.0457	-.0062	$\sim \frac{1}{7.5}$
P_2^2	+.209	+.0869	$\sim \frac{1}{2.5}$
P_4^0	+.00237	-.0004	$\sim \frac{1}{5}$

P_4^2	+.0629	+.11	$\sim$ 2
P_4^4	+.712	+.629	$\sim$ 1

This tabulation shows that the cancellation is very high for P_2^o, P_2^2 and P_4^o and relatively smaller for P_4^2 and P_4^4.

On the basis of this crude approximation, it is tempting to make some speculations about the relation between crystal structure and the spectra of paramagnetic ions in the crystal. The example of $BaSO_4$ shows that a large ion with high coordination is placed in a crystalline field which can be regarded as a spherically symmetric field with relatively small components of lower symmetry. The lowest order components will tend to have the smallest amplitude. In addition, the large distances to the nearest neighbors will tend to reduce the amplitudes of the lowest order terms still farther. This type of field will tend to produce poor quenching of the orbital moment and also small zero-field splittings.

One of the reasons for choosing barite for investigation was the low symmetry about the cation sites. It was believed that the low symmetry made a large zero-field splitting more likely. It was also believed that more orbital degeneracies would be removed, leaving the orbital ground state a singlet for most ions. It appears probable that these considerations were incorrect. The zero-field splitting results primarily from the second-order terms in the spin-Hamiltonian. These terms would tend to be

small for crystals such as barite. The orbital degeneracies are removed, but the magnitude of the splittings of the orbital levels would be generally smaller than in crystals with smaller coordination.

3.3 The Spin-Hamiltonian in Barite

The irregular nature of the crystalline field computed above makes it impossible to make any reasonable estimate of the nature of the spectrum of paramagnetic impurities. In particular, P_4^o in the crystalline field was very small due to mutual cancellation of contribution from the nearest neighbors. The sign of this term normally determines the ground state. In the case of $BaSO_4$, the magnitude is so small that the ground state would be unknown even if the sign of the term were known. Only the form of the spin-Hamiltonian can be given. It is

$$\mathcal{H}_s = DS_z^2 + E(S_x^2 - S_y^2) + \text{quartic terms}$$

It is customary to neglect higher fourth order terms when lower order terms of the same symmetry exist in the spin-Hamiltonian. This is because the quartic terms are expected to be substantially smaller and are difficult to measure in the presence of a larger effect of the same symmetry.

The symmetry of the spin-Hamiltonian is orthorhombic, in spite of the fact that the actual point symmetry is only m (monoclinic). This is because only even order terms are allowed in the spin-Hamiltonian. The requirement of a horizontal reflection symmetry forces the spin-Hamiltonian to have vertical reflection

symmetry as well.

3.4 Experimental Results

Samples of barite from England, Colorado and South Dakota were used for measurements of paramagnetic resonance. The samples from England are clear, free of fractures and very large. They were cleaved and cut into pieces of approximately 1 cc. The Colorado samples are light blue, single crystals of about 1/2 cc. The crystals are very well-formed, and the axes could be identified without cleaving. The South Dakota samples are amber and not as well-formed as those from the other sources. A spectrographic analysis on the samples by G. Gordon showed the following impurities:

Source	Fe	Cr	Sr
England	$<$ .001	$<$ .001	.2
Colorado	$<$ .001	.005	.2
S. Dakota	$<$ .001	$<$ .001	.2

$BaSO_4$ is isomorphous with $PbSO_4$ and $SrSO_4$. Sr^{2+} is a very common impurity in $BaSO_4$. Barite is also found to contain moderate amounts of FeO. A report on the analysis of barite from the same source which provided the crystals used here shows typically 1% of FeO[76]. Therefore, iron is the most likely paramagnetic ion in $BaSO_4$.

The samples were checked for paramagnetic resonance at both x-band and k-band. All samples show a large number of

extremely narrow lines in the region of free spin resonance. In addition, the samples from Colorado show a broad line at $g \sim 1.98$. The intensity indicates a concentration of about 10^{17}/cc. This broad line is not isotropic and could be a $m_s = +1/2 \longleftrightarrow -1/2$ transition of some ion with a half-integral spin. However, no other line was detected at x-or k-band. No effort was made to investigate it further.

The narrow lines are not of interest for three-level masers. However, they were examined in some detail because of their unusually narrow line width. At 77°K, the line width was .06 gauss. They are saturated with about .5 mw of microwave power at room temperature. With a Q of 1000, the relaxation T_1 is computed to be 30 μs at room temperature.

These lines are removed by heating but show a gradual recovery over a period of many months. Similar lines are produced by x-ray or neutron irradiation.

The behavior of the sharpest lines was examined with very low microwave power ($<$.1 mw). The lines are almost, but not quite, isotropic. The maximum variation for various orientations of the magnetic field is about 1 gauss. The line splits into two lines whenever the magnetic field is not parallel to one of the glide planes. The variation is distinctly orthorhombic. Spin-echo was attempted with these lines. At 77°K, none was observed. At 4.2°K, echoes were observed. T_{12} was estimated to be 50 μs. The echoes were marginal, possibly due to excessive Q or insufficient spin concentration.

CONCLUSION

The spectra of Fe^{3+} and very probably Cr^{3+} in calcite were examined. The zero-field splittings in the two spectra were 6.55 gc and 11.03 gc for Fe^{3+} and 3.32 gc for Cr^{3+}. There is a large discrepancy in the measured g-values. No explanation could be given to account for this difficulty. The relaxation time for Fe^{3+} is estimated to be 50 μs at 77°K. An accurate estimate could not be made because the entire sample could not be saturated at once. Therefore, a clear-cut boundary for saturation could not be found.

The zero-field splittings in calcite are smaller than those found in corundum. The value for Fe^{3+} in calcite is about 1/2 of the value in corundum. The value for Cr^{3+} is almost 1/4. The zero-field splitting of Mn^{2+} in calcite is likewise about 1/2 of that in corundum.[77] In this very important respect, calcite is inferior to corundum as a maser material.

The relaxation time of Fe^{3+} in calcite seems comparable to that of Fe^{3+} in corundum. Only a rough estimate was given.

The line width in calcite is not increased by nuclear moments in the host lattice. In this respect, calcite holds an advantage over corundum which has a large nuclear moment associated with Al^{3+}.

As a three-level maser the smaller line widths found in calcite are not a sufficient advantage to make it a choice over corundum. If successfully synthesized, the spectrum of Fe^{3+} in

calcite is best suited for a zero-field, or a very low-field maser, operating with a signal frequency of about 6.5 gc with a pump frequency of 17.5 gc. The spectrum of Cr^{3+} is not useful.

The measured values reported here are not as accurate as the values reported for paramagnetic spectra by other researchers in the field. This is due to a limitation in experimental methods imposed by the small concentration of the imputities observed and the lack of a larger magnet.

It is doubtful that the results presented here are of sufficient interest to encourage concentrated efforts to grow calcite as a maser material. However, as a host for the study of paramagnetic ions, it provides a trigonal site which can be valuable for the study of the Jahn-Teller effect in Cu^{2+} and Cr^{2+}. The zero-field splittings measured in Fe^{3+}, Cr^{3+} and Mn^{2+} are relatively small. The large number of other small lines observed at x-band between 0 and 5000 gauss suggests that the complete spectrum of many other ions can be observed in calcite.

The spectrum of iron in $BaSO_4$ was expected, but none was observed. It is probable that, if any iron were present, it was in the divalent state. The relaxation time was probably very short and the energy levels scattered over many wave members.

The examination of the local symmetry and crystalline field of barite indicates that the large ionic radius of the cation and the high coordination number is not likely to result in a good maser material. It seems likely that the best combination of large zero-field splitting and good quenching of the orbital

moment (and, as a consequence, long relaxation time) is obtained by choosing a crystal whose cation has as low a coordination number as possible and a low point symmetry. It is interesting to observe that TiO_2 (rutile) comes fairly close to satisfying these conditions.

REFERENCES

1. J. P. Gordon, H. J. Geiger and C. H. Townes, Phys. Rev. 99, 1264 (1955).

2. S. Foner, Phys. Rev. Letters 3, 36 (1960).

3. J. S. Thorp, Report at the Second International Quantum Electronics Conference, 1961.

4. N. Bloembergen, Phys. Rev. 104, 324 (1956).

5. N. G. Bassov and A. M. Prokhorov, J. Exptl. Theor. Phys. 27, 4131 (1954).

6. A. L. McWhorter and J. W. Meyers, Phys, Rev. 109, 312 (1958).

7. C. Kikuchi, J. Lambe, G. Makhov and R. W. Terhune, Journal of Applied Physics 30, 1061 (1959).

8. J. E. Geusic, M. Peters and E. O. Schultz-DuBois, Bell System Technical Journal 38, 291 (1959).

9. S. Foner, L. R. Momo et al., Report in the Second International Quantum Electronics Conference, 1961.

10. D. L. Carter and A. Okaya, Phys. Rev. 118, 1485 (1960).

11. S. Foner and L. R. Momo, Journal of Applied Physics 31, 742 (1960).

12. M. Peter, L. G. Van Uitert and J. B. Mock, Report at the Second International Quantum Electronics Conference, 1961.

13. C. F. Hempstead and K. D. Bowers, Phys. Rev. 118, 131, (1960).

14. J. C. Kemp, Ph.D. Thesis, University of California, 1960.

15. J. H. Van Vleck, Theory of Electric and Magnetic Susceptibilities, Oxford University Press, 1932.

16. E. J. Zaviosky, Journal of Physics (U.S.S.R.) 9, 211 (1945).

17. B. Bleaney and K. W. H. Stevens, Reports on the Progress in Physics, 16, 108 (1953).

18. W. Low, Paramagnetic Resonances in Solids. Solid State Physics Suppl. 2. Academic Press, 1960.

19. G. F. Koster and H. Statz, Phys. Rev. 113, 445 (1959).

20. K. D. Bowers and J. Owen, Reports on the Progress in Physics 18, 304 (1955).

21. J. W. Orton, Report on the Progress in Physics 22, 204, (1959).

22. E. U. Condon and G. H. Shortley, The Theory of Atomic Spectra, Cambridge University Press, 1957.

23. W. Low, Hebrew University, Dept. of Physics, Tech. Note No. 16.

24. K. W. H. Stevens, Proc. Phys. Soc. 65A, 209 (1952).

25. R. J. Elliot and K. W. H. Stevens, Proc. Roy. Soc. A218, 553 (1953).

26. A. Abragam and M. H. L. Pryce, Proc. Roy. Soc. A205, 135, (1951).

27. H. A. Kramers, Proc. Amsterdam Acad. Science 33, 959 (1930).

28. M. Tinkham, Proc. Roy. Soc. A236, 549 (1956).

29. J. H. Van Vleck, Phys. Rev. 41, 208 (1935).

30. K. Ono, S. Koide, H. Sekiyama and H. Abe, Phys. Rev. 96, 38 (1954).

31. H. A. Jahn and E. Teller, Proc. Roy. Soc. A161, 220 (1937).

32. J. H. Van Vleck, Journal of Chemical Physics 7, 72 (1939).

33. B. Bleaney, K. D. Bowers and R. S. Trenham, Proc. Roy. Soc. A228, 157 (1955).

34. G. F. Koster, Quarterly Prog. Report, Solid State and Molecular Theory Group. Massachusetts Inst. of Tech. October 15, 1958.

35. G. W. Ludwig and H. H. Woodbury, Phys. Rev. Letters 5, 468 (1960).

36. J. H. Van Vleck, Phys. Rev. 57, 426 (1940).

37. F. Bloch, Phys. Rev. 70, 460 (1946).

38. A. G. Redfield, Phys. Rev. 98, 1787 (1955).

39. S. Hartmann, Ph.D. Thesis, University of California, 1961.

40. R. W. Terhune, Symposium on Masers, U. of Michigan, 1959.

41. G. S. Bogle and A. Symmons, Australian Journal of Physics 12, 1 (1959).

42. L. S. Kornienko and A. M. Prokhorov, JETP 36, 919 (1959).

43. G. S. Bogle, Proc. I.R.E. 49, 567 (1961).

44. J. R. Singer, Masers, John Wiley and Sons, Inc., N.Y., 1959.

45. W. L. Bragg, The Atomic Structure of Minerals, Cornell University Press, 1937.

46. S. Geschwind and J. P. Remeika, Phys. Rev. 122, 757 (1961).

47. Handbook of Chemistry and Physics, U. S. Rubber Publishing Co., Cleveland, Ohio, 1958.

48. R. W. G. Wyckoff, Crystal Structures, Interscience Publishers, Inc., New York, 1957.

49. Private discussion with Professor Pabst, Dept. of Geology, University of California.

50. E. L. Hahn, Phys. Rev. 80, 580 (1950).

51. P. P. Pashnin and A. M. Prokhorov, Soviet Physics 7, 535 (1958).

52. B. Bolger and B. J. Robinson, Physica 26, 133 (1960).

53. R. A. Armstrong and A. Szabo, Canadian Journal of Physics 38, 1304 (1961).

54. J. H. Pace, D. F. Sampson and J. S. Thorp, Phys. Rev. Letters 4, 18 (1960).

55. R. E. Michel, Phys. and Chem. of Solids 13, 165 (1960).

56. A. George and D. T. Teaney, Review of Scientific Instruments 31, 997 (1960).

57. C. Kikuchi, Resonance Absorption in Paramagnetic Ion with Spin 5/2, $CaCO_3$:Mn, University of Michigan Willow Run Lab. Tech. Memorandum, 2616-10-R (1959).

58. H. M. Evjen, Phys. Rev. 39, 675 (1932).

59. C. Kittel, Introduction to Solid State Physics, John Wiley and Sons, Inc., New York, 1956.

60. J. M. Baker, B. Bleaney and W. Hayes, Proc. Roy. Soc. A247, 141 (1958).

61. W. R. Smythe, Static and Dynamic Electricity, McGraw-Hill Book Co., New York, 1950.

62. B. Bleaney and R. S. Trenham, Proc. Roy. Soc. 223, 1 (1954).

63. A. M. Prokhorov and L. S. Kornienko, JETP 6, 620 (1958).

64. H. H. Woodbury, Phys. Rev. 118, 1286 (1960).

65. B. R. Judd, Proc. Roy. Soc. A232, 458 (1955).

66. R. J. Elliot and K. W. H. Stevens, Proc. Roy. Soc. A219, 387 (1953).

67. C. A. Hutchinson, Jr., B. R. Judd and D. F. O. Pope, Proc. Phys. Soc. B70, 541 (1957).

68. H. Watanabe, Prog. Theor. Phys. (Kyoto) 18, 405 (1957).

69. C. Palache, H. Berman and C. Frondel, Dana's System of Minerology, John Wiley and Sons, Inc., New York, 1955.

70. T. Maiman, Quantum Electronics, 324, Columbia University Press, 1960.

71. F. K. Hurd, M. Sachs and W. D. Hirschberger, Phys. Rev. 93, 373 (1954).

72. A. E. Siegman and W. S. C. Chang, Characteristics of Ruby for Maser Applications, Stanford Electronics Lab. Tech. Report No. 156-2 (1958).

73. B. Bleaney, Private discussion.

74. B. Bleaney, H. E. D. Scovil and R. S. Trenham, Proc. Royal Soc. A223, 15 (1954).

75. R. W. James and W. A. Wood, Proc. Roy. Soc. A109, 617 (1925).

76. K. C. Dunham, Geological Survey of Great Britain. Geology of the Northern Pennine Ore Field, Vol. 1, p. 130, His Majesty's Stationary Office, 1948.

77. W. Low, Phys. Rev. 119, 132 (1960).

78. J. S. Griffith, The Theory of Transition Metal Ions, Cambridge University Press, 1961.

79. R. D. Mattuck and M. W. P. Strandberg, Phys. Rev. 119, 4 (1960).

80. L. K. Wanlass and J. Wakabayashi, Phys. Rev. Letters 6, 271 (1961).

AIR FORCE OFFICE OF SCIENTIFIC RESEARCH
ELECTRON TUBE RESEARCH
CONTRACT NO. AF 49(638)-102

DISTRIBUTION LIST

ADDRESSEE	NO. COPIES
AFOSR ATTN: Technical Library Washington 25, D. C.	2
AFOSR (SRPP) Washington 25, D. C.	3
ASD ATTN: Technical Library Wright-Patterson AFB, Ohio	1
AFCRL ATTN: Technical Library L. G. Hanscom Field Bedford, Massachusetts	1
EOAR The Shell Building 47 Rue Cantersteen Brussels, Belgium	(Unclassified Reports) 1
ARL ATTN: Technical Library Wright-Patterson AFB, Ohio	1
ASTIA (TIPCR) Arlington Hall Station Arlington 12, Virginia	10
Director of Research Headquarters, USAF ATTN: AFRDR Washington 25, D. C.	1
Office of Naval Research Department of the Navy ATTN: Code 420 Washington 25, D. C.	1
Naval Research Laboratory ATTN: Technical Library Washington 25, D. C.	1
Chief of Research and Development ATTN: Scientific Information Branch Department of the Army Washington 25, D. C.	1
Chief, Physics Branch Division of Research U. S. Atomic Energy Commission Washington 25, D. C.	1
U. S. Atomic Energy Commission Technical Information Extension P. O. Box 62 Oak Ridge, Tennessee	1
National Bureau of Standards ATTN: Technical Library Room 203, Northwest Building Washington 25, D. C.	1
Physics Program National Science Foundation Washington 25, D. C.	1
Director, Army Research Office, Durham Box CM, Duke Station Durham, North Carolina	1
AEDC (AEOIM) ATTN: Technical Library Arnold Air Force Station Tullahoma, Tennessee	1
AFFTC (AFOTL) ATTN: Technical Library Edwards AFB, California	1
AFMDC (MDF) Holloman AFB, New Mexico	1
AFMDC (HDOI) Holloman AFB, New Mexico	1
ARGMA (ORDXR-OTL) Redstone Arsenal, Alabama	1
Institute of Technology (AU) Library MCLI-LIB, Bldg. 125, Area B Wright-Patterson AFB, Ohio	1
AFSC (SCRS) Andrews AFB Washington 25, D. C.	1
Signal Corps Engineering Laboratory ATTN: (SIGFM/EL-RPO) Fort Monmouth, New Jersey	1
Headquarters National Aeronautics and Space Administration ATTN: Technical Library Washington 25, D. C.	1
Ames Research Center (NASA) ATTN: Technical Library Moffett Field, California	1
Technical Information Division Bldg. 30, Room 101 Radiation Laboratory Berkeley, California	1
Hans Motz Oxford University Oxford, England	1
Miss May Dorin Department of Archives 303 Library University of California Berkeley 4, California	1
High Speed Flight Station (NASA) ATTN: Technical Library Edwards AFB, California	1
Langley Research Center (NASA) ATTN: Technical Library Langley AFB, California	1
Lewis Research Center (NASA) ATTN: Technical Library 21000 Brookpark Road Cleveland 35, Ohio	1
Goddard Space Flight Center (NASA) ATTN: Technical Library Greenbelt, Maryland	1
George C. Marshall Space Flight Center (NASA) ATTN: Technical Library Redstone Arsenal, Alabama	1
Wallops Station (NASA) ATTN: Technical Library Wallops Island, Virginia	1
Institute of Aeronautical Sciences 2 East 64th Street New York 21, New York	(Unclassified Reports) 1
Applied Mechanics Reviews Southwest Research Institute 8500 Culebra Road San Antonio 6, Texas	(Unclassified Reports) 1
Linda Hall Library ATTN: Document Division 5109 Cherry Street Kansas City 10, Missouri	(Unclassified Reports) 1
AFOSR (SRAL) ATTN: Technical Library Holloman AFB, New Mexico	2
AFSWC (SWOI) Kirtland AFB, New Mexico	1
Advanced Research Projects Agency Washington 25, D. C.	1
Rand Corporation 1700 Main Street Santa Monica, California	1
Chairman Canadian Joint Staff (DRB/DSIS) 2450 Massachusetts Avenue, N.W. Washington 25, D. C.	(Unclassified Reports) 1
Officer in Charge Office of Naval Research Navy No. 100 Fleet Post Office New York, New York	1
Office of Technical Services Department of Commerce Technical Reports Branch Washington 25, D. C.	1
M. D. Adcock, Head American Systems Incorporated 1625 E. 126 Street Hawthorne, California	1
Dr. Harold Glaser Office of Naval Research Washington 25, D. C.	1
Professor Charles Townes Department of Physics Columbia University New York 27, New York	1
Professor Harvey Brooks Department of Physics Harvard University Cambridge 38, Massachusetts	1
Professor P. Kusch Department of Physics Columbia University New York 27, New York	1
Professor N. Bloembergen Department of Physics Harvard University Cambridge 38, Massachusetts	1
Dr. Irving Rowe Office of Naval Research 346 Broadway New York, New York	1
W. A. Kozumplik, Manager Lockheed Aircraft Corporation Missiles and Space Division Technical Information Center 3251 Hanover Street Palo Alto, California	1
Mr. E. Okress Sperry Gyroscope Company Electron Tube Division Mail Station 1 B40 Great Neck, New York	1
DOFL (ORDTL 012) Washington 25, D. C.	1
Prof. J. H. Mulligan, Jr. Chairman, Department of Electrical Engineering New York University 25 Waverly Place New York, New York	1
The Ohio State University Antenna Laboratory 2024 Neil Avenue Columbus 10, Ohio ATTN: Security Officer	1
Major General Casemiro Montenegro Filho Central Técnico da Aeronáutica (CTA) São José dos Campos São Paulo, Brasil	1
Purdue University Lafayette, Indiana ATTN: Richard L. Funkhouser Engineering Librarian	1
Professor J. Van Bladel Electrical Engineering Department College of Engineering University of Wisconsin Madison 6, Wisconsin	1
Professor W. Low Department of Physics The Hebrew University of Jerusalem Jerusalem, Israel	1
University of Illinois Department of Electrical Engineering Urbana, Illinois ATTN: H. Von Foerster	1
Ohio State University Department of Electrical Engineering Columbus, Ohio	1
The University of Michigan Department of Electrical Engineering Electron Physics Laboratory Ann Arbor, Michigan ATTN: Professor J. E. Rowe	1
Stanford University Electronics Research Laboratory Stanford, California	1
Massachusetts Institute of Technology Research Labs. of Electronics Room 20B-221, Document Office Cambridge 39, Massachusetts ATTN: J. H. Hewitt	1
Harvard University Cruft Laboratory Cambridge 38, Massachusetts ATTN: Technical Reports Collection	1
Technical Information Libraries Bell Telephone Laboratories, Inc. Whippany Laboratory Whippany, New Jersey ATTN: Technical Reports Librarian	1
California Institute of Technology Pasadena 4, California ATTN: R. Gould	1
Sylvania Electric Company Mountain View, California ATTN: D. H. Goodman	1
Professor William H. Surder Electrical Engineering Department Princeton University Princeton, New Jersey	1
General Electric Company Electron Tube Div. of the Research Lab. The Knolls Schenectady, New York ATTN: E. D. McArthur	1
General Electric Company Missile and Space Vehicle Department 3198 Chestnut Street Philadelphia 4, Pennsylvania ATTN: Aerodynamics Engineering Operation R. F. Peck, Manager	1
Hughes Aircraft Company Florence at Teale Street Culver City, California ATTN: Documents Group, Bldg. 6, Rm. X2015	1
RCA Laboratories Princeton, New Jersey ATTN: Dr. W. M. Webster, Director Electronics Research Labs.	1
Varian Associates 611 Hansen Way Palo Alto, California ATTN: Technical Library	1
Westinghouse Electric Corporation Electronic Tube Division P. O. Box 284 Elmira, New York ATTN: Mr. Sheldon S. King, Librarian	1
Professor Zohrab Kaprielian University of Southern California School of Engineering Department of Electrical Engineering University Park Los Angeles 7, California	1
B. J. Maxum Dalmo-Victor Research Laboratories Belmont, California	1
Headquarters Air Force Office of Scientific Research Office of Aerospace Research USAF Washington 25, D. C. ATTN: Marshall C. Harrington General Physics Division	1